ACS ENVIRONMENTAL Au
AN OPEN ACCESS JOURNAL OF THE AMERICAN CHEMICAL SOCIETY

pubs.acs.org/environau
Review

Photocatalytic Conversion of Methane: Current State of the Art, Challenges, and Future Perspectives

Published as part of the ACS Environmental Au virtual special issue "2023 Rising Stars in Environmental Research".

Zhuo Liu,[#] Biyang Xu,[#] Yu-Jing Jiang, Yang Zhou, Xiaolian Sun, Yuanyuan Wang, and Wenlei Zhu*

Cite This: ACS Environ. Au 2023, 3, 252−276

ABSTRACT: With 28−34 times the greenhouse effect of CO_2 over a 100-year period, methane is regarded as the second largest contributor to global warming. Reducing methane emissions is a necessary measure to limit global warming to below 1.5 °C. Photocatalytic conversion of methane is a promising approach to alleviate the atmospheric methane concentrations due to its low energy consumption and environmentally friendly characteristics. Meanwhile, this conversion process can produce valuable chemicals and liquid fuels such as CH_3OH, CH_3CH_2OH, C_2H_6, and C_2H_4, cutting down the dependence of chemical production on crude oil. However, the development of photocatalysts with a high methane conversion efficiency and product selectivity remains challenging. In this review, we overview recent advances in semiconductor-based photocatalysts for methane conversion and present catalyst design strategies, including morphology control, heteroatom doping, facet engineering, and cocatalysts modification. To gain a comprehensive understanding of photocatalytic methane conversion, the conversion pathways and mechanisms in these systems are analyzed in detail. Moreover, the role of electron scavengers in methane conversion performance is briefly discussed. Subsequently, we summarize the anthropogenic methane emission scenarios on earth and discuss the application potential of photocatalytic methane conversion. Finally, challenges and future directions for photocatalytic methane conversion are presented.

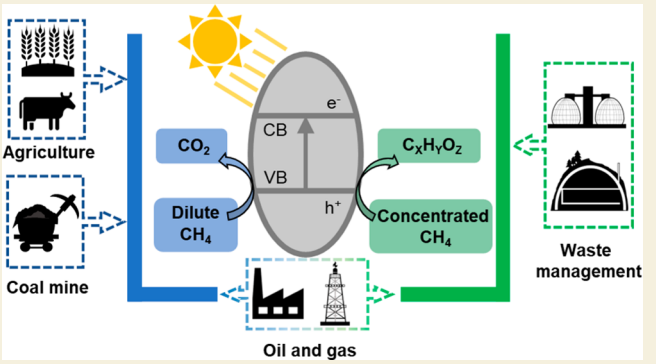

KEYWORDS: *greenhouse effect, methane emission, photocatalytic conversion, photocatalyst design, semiconductor, cocatalyst, electron scavengers, application scenarios*

1. INTRODUCTION

Global warming caused by greenhouse gases (GHGs) is a clear threat to human societies and requires urgent action. As the second most important contributor to GHG emissions in the world, methane has attracted great attention in recent years.[1,2] According to the relevant reports, the atmospheric methane concentration has more than doubled since preindustrial time (1879 vs 722 ppb), and the current methane emissions account for almost 25% of atmospheric warming.[3,4] Despite its lower atmospheric concentration compared to that of CO_2 (417 ppm), methane is a potent greenhouse gas 28−34 times more powerful than CO_2 in warming the atmosphere over a 100-year time period (per unit mass).[5,6] In addition to its direct radiative forcing on the climate, methane is also a major precursor of ground-level ozone, which causes about 500,000 premature deaths worldwide each year.[7] From an economic perspective, leaked methane can lead to labor losses, high healthcare costs for asthma-related illnesses, and crop yield decline, resulting in an economic loss of around US $450 billion each year.[8] Therefore, it is essential to reduce atmospheric methane concentrations as soon as possible, which provides an opportunity to meet the Paris Agreement's goal of limiting the temperature rise to 1.5 °C.[7,9] Recently, the United Nations Environment Programme has published the Global Methane Assessment to highlight the importance of reducing methane emissions.[8] In addition, the U.S. Department of Energy announced a US $35 million grant to develop technologies to reduce methane emissions from the oil, natural gas, and coal industries.

Received: February 14, 2023
Revised: May 24, 2023
Accepted: June 2, 2023
Published: June 20, 2023

Currently, technologies to reduce methane emissions can be broadly categorized into methane capture and storage technologies, direct combustion, and methane reutilization. There are some applicable circumstances for the capture and storage technologies. For example, in oil and gas industry, the methane capture and storage technologies are partly similar to carbon dioxide capture and storage technologies, and captured natural gas can be injected into the oilfields to enhance oil recovery like pressurized CO_2.[10,11] However, they may face similar implementation dilemmas of energy consumption, operating costs, and maintenance-related safety issues that happen to carbon dioxide capture and storage technologies.[10,12] Direct combustion of methane may not be sufficient, especially for dilute methane-air flows, which results in extra carbon dioxide emissions, unignited methane leakage, and possible air pollutant emissions, and it is an environmentally unfriendly process that is planned to be phased out gradually.[13] Unlike the above two technologies, methane reutilization has great potential to produce chemical commodities without the use of crude oil and to reduce environmental pollution caused by methane. However, methane is a highly stable molecule with a symmetrical tetrahedral configuration, and this nonpolar structure endows methane with extremely high C−H bond energy (439 kJ mol^{-1}), low polarizability (2.84×10^{-40} C^2 m^2 J^{-1}), and low electron and proton affinity (−1.9 eV and 543.9 kJ mol^{-1}, respectively).[14,15] As a result, the catalytic conversion of methane usually requires high temperatures and harsh reaction conditions.[16,17] Methane can be oxidized to CO_2 or selectively oxidized to various valuable chemicals (CH_3OH, CH_3CH_2OH, C_2H_6, and C_2H_4). From the point of view of climate mitigation and environment benefit, all these conversion processes can offset some of the global warming caused by methane in the near term. But from the perspective of chemical production and energy sustainability, the conversion process to high-value chemicals and fuels can further increase the economic value of methane, which is attractive to the industry and market. However, this process is hampered by the overoxidation of methane to CO_2, as CO_2 is a more thermodynamically stable but undesirable product from the perspective of product value.[18−20] Therefore, the conversion of methane into valuable products with high selectivity under mild conditions remains a significant challenge.

To date, many technologies have been utilized for methane conversion, and they now include thermocatalytic technologies, electrocatalytic technologies, plasma technologies, membrane technologies, and so on.[21−24] However, traditional thermocatalytic technologies, such as traditional Cu/Fe-based zeolite thermocatalysis, usually requires strong and high-cost oxidants (H_2O_2, N_2O) to achieve a large methane conversion.[25] Besides, a high temperature is basically needed for thermodynamically unfavorable methane conversions, such as nonoxidative coupling of methane. The high temperature can lead to the formation of carbon or coke, resulting in the fast deactivation of the catalyst.[26] Electrocatalytic technologies, such as the methane solid oxide fuel cell, also need to operate at temperatures above 500 °C because electrochemical methane oxidation at low temperatures is extremely sluggish, and the product of the fuel cell is CO_2 instead of high-value chemicals.[27] Comparatively, photocatalytic methane conversion is emerging as an ideal method to achieve methane conversion under mild conditions.[28−31] First, it uses solar energy, a green and renewable source, to activate methane, turning a primary energy source into chemical energy.[32] Second, the energetic carriers (electrons and holes) generated by photocatalysts absorbing photons can activate and convert methane by transferring their energy or charge to methane, thus breaking the thermodynamic equilibrium and allowing the uphill reactions to occur at room temperature.[33] Third, ambient temperatures can avoid the deactivation of catalysts to some extent. However, the inherent inertness of methane molecules, the disadvantages of bulk semiconductors, and the overoxidation of products limit the efficiency and selectivity of photocatalytic methane conversion. In semiconductors, the charge recombination (μs) is much faster than participation in redox reactions (ms), resulting in severe charge recombination in the bulk phase and on the surface.[34] To address these issues, several engineering strategies have received considerable attention, including morphology control, heteroatom doping, facet engineering, cocatalyst modification, and utilization of electron scavengers (Figure 1). These strategies can enhance the absorption of light, improve the separation efficiency of photogenerated carriers, and provide more reactive sites for methane adsorption and activation, which can improve the activity of methane conversion. Furthermore, surface site engineering, such as heteroatom doping, facet engineering, and cocatalyst modification, can regulate the adsorption energy and desorption ability of intermediates and products, realizing high selectivity toward desired products.

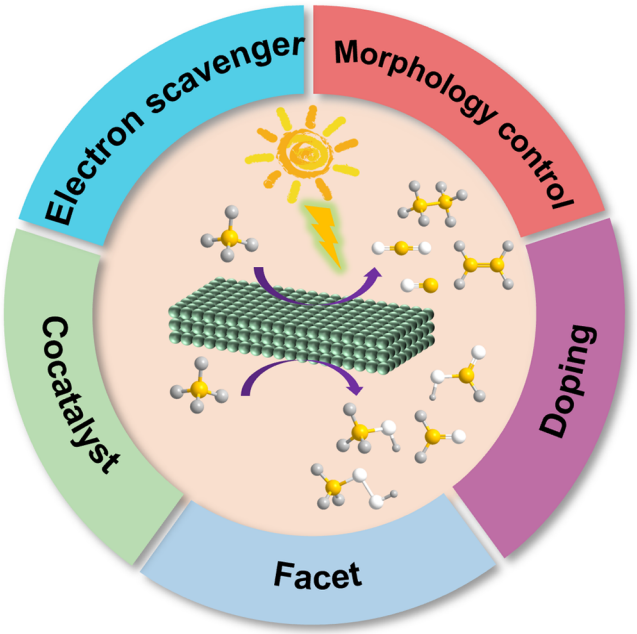

Figure 1. Outline of emerging strategies for photocatalytic methane conversion.

In order to reduce the atmospheric methane concentration through the energy-efficient and eco-promising photocatalytic process, great efforts have been made to exploit efficient systems for photocatalytic methane conversion.[32,35] However, the mechanisms over different catalysts still require full consideration and analysis. In addition, the application potential of photocatalytic methane conversion in different methane emission scenarios, which is of great importance for its future practical application, has not been discussed. In this review, we provide an overview about the photocatalyst and

https://doi.org/10.1021/acsenvironau.3c00002
ACS Environ. Au 2023, 3, 252−276

system design strategies for the photocatalytic methane conversion process (including the design of semiconductors through morphology control, heteroatom doping, facet engineering, cocatalyst modification, and utilization of electron scavengers), describing how these strategies affect performance, mechanisms, and pathways. Furthermore, we summarize the anthropogenic methane emission scenarios on earth and analyze the application potential of photocatalytic methane conversion in these scenarios. Finally, we outline key challenges and perspectives for photocatalytic methane conversion. We hope that this review can provide valuable guidance for the development of desirable photocatalytic methane conversion systems and inspiration for the treatment of produced methane.

2. FUNDAMENTALS OF PHOTOCATALYTIC CONVERSION OF METHANE

Under light irradiation with energy higher than the bandgap energy (E_g) of the semiconductor, the electrons on the valence band (VB) can be excited to the conduction band (CB), together with the generation of holes on the VB. The generated separated electrons and holes can migrate to the surface of the semiconductor and then participate in the redox reactions.[32] Therefore, the efficiency of photocatalytic methane conversion is determined by three key parameters and can be described as $\eta_{total} = \eta_{abs} \times \eta_{cs} \times \eta_{redox}$, where η_{abs}, η_{cs}, and η_{redox} denote the photoabsorption efficiency, carrier separation efficiency, and surface reaction efficiency, respectively. Accordingly, considerable efforts should be made to design photocatalysts with strong photoabsorption ability, efficient carrier separation ability, and abundant active sites for methane conversion.[36] Yet it is worth noting that there are differences between the photocatalysts for methane conversion and contaminants oxidation. For oxidation of contaminants, photocatalysts that can efficiently activate H_2O to $^{\bullet}OH$ are usually needed to realize the complete abatement of pollutants (into CO_2, H_2O, or at least harmless products).[37] For methane conversion, an ideal catalyst should be able to achieve partial oxidation of methane to high-value products rather than to the oxidation of CO_2, in order to improve the utilization value of methane. In order to improve the selectivity of high-value products, it is necessary to introduce suitable active sites to regulate the formation of free radicals, the activation barriers of intermediates, and the adsorption/desorption of intermediates. Besides, photocatalysts for methane oxidation need to have efficient methane activation capability.

The activation of the highly stable C−H bonds of methane is regarded as the rate-determining step for methane conversion.[38,39] The activation of the C−H bond follows two main pathways, including direct and indirect pathways (Figure 2). The VB of metal oxides (TiO_2, ZnO) is mainly composed of O 2p orbitals, which possess quite positive potential (ca. +3.0 V vs SHE) and offer strong oxidation ability for the activation of CH_4 ($CH_4/^{\bullet}CH_3$: 0.83 V). Upon light irradiation, surface lattice oxygen of these metal oxides can trap photoinduced holes (h^+), leading to the generation of reactive oxygen species (O^-), which can be characterized by in situ electron paramagnetic resonance (EPR) spectra. O^- active species can directly capture the H atom from CH_4 and generate $^{\bullet}CH_3$ ($CH_4 + M^{(n-1)+}-O^- \rightarrow {}^{\bullet}CH_3 + M^{(n-1)+}-OH$).[17,40,41] Interestingly, recent work by Hu's group revealed that the C−H bond can also be activated directly by the photoexcited electrons accumulated on the cocatalyst.[42] As for

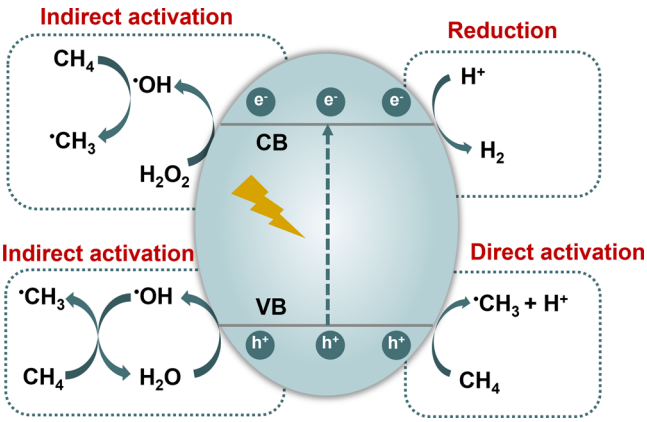

Figure 2. Schematic illustration of the methane activation mechanism over semiconductor-based photocatalysts.

the indirect route, the C−H bond cleavage can be switched on by the generated oxygen radicals, such as $^{\bullet}OH$.[43] The highly oxidative $^{\bullet}OH$ species can be generated through the reaction between photoinduced carriers and adsorbate (H_2O and H_2O_2, $H_2O + h^+ \rightarrow {}^{\bullet}OH + H^+$; $H_2O_2 + H^+ + e^- \rightarrow {}^{\bullet}OH$), which can capture an H atom from methane.

Methane can be converted into a variety of products by photocatalysis including gaseous products (C_2H_6, C_2H_4, and C_3H_8) and liquid products (CH_3OOH, CH_3OH, CH_3CH_2OH, HCHO, and HCOOH). The type of products is related to the reaction systems. For example, C_2H_6 and C_2H_4 have high economic values are usually the target products via oxidative coupling of methane ($4CH_4 + O_2 \rightarrow 2C_2H_6 + 2H_2O$, $\Delta G^0_{298\ K} = -320$ kJ mol^{-1}) or nonoxidative coupling of methane ($2CH_4 \rightarrow C_2H_6 + H_2$, $\Delta G^0_{298\ K} = 68.6$ kJ mol^{-1}) under gas−solid reaction conditions, whereas liquid oxygenates can be synthesized via partial oxidation of methane under liquid−solid reaction conditions. For liquid−solid reactions, the $^{\bullet}CH_3$ radical tends to react with $^{\bullet}OOH$ ($O_2 + e^- + H^+ \rightarrow {}^{\bullet}OOH$) to form CH_3OOH in the presence of O_2, which can be reduced to CH_3OH and then oxidized to $HCHO/CO_2$. Besides, the $^{\bullet}CH_3$ radical can also react with $^{\bullet}OH$ or H_2O to generate CH_3OH.[31,44,45] The selectivity of liquid products is related to their ability to desorb on the catalyst surface. In addition, syngas (CO and H_2) can be obtained through methane reforming with H_2O (gas) or CO_2, which are known as steam reforming of methane ($CH_4 + H_2O \rightarrow 3H_2 + CO$, $\Delta G^0_{298\ K} = 142$ kJ mol^{-1}) and dry reforming of methane ($CH_4 + CO_2 \rightarrow 2H_2 + 2CO$, $\Delta G^0_{298\ K} = 171$ kJ mol^{-1}), respectively.[46−48] In general, the conversion processes are thermodynamically unfavorable without the participation of oxygen, such as nonoxidative coupling of methane, steam reforming of methane, and dry reforming of methane. These processes can be driven under mild conditions by the photo energy supplied.

3. STRATEGIES TO IMPROVE METHANE PHOTOCONVERSION PERFORMANCE

3.1. Design of Semiconductors

Semiconductors are a crucial component of photocatalysts, which are responsible for light absorption to generate electron−hole pairs. For the photocatalytic conversion of methane, the electrons and/or holes on the CB/VB of a semiconductor should be able to drive the corresponding

https://doi.org/10.1021/acsenvironau.3c00002
ACS Environ. Au 2023, 3, 252−276

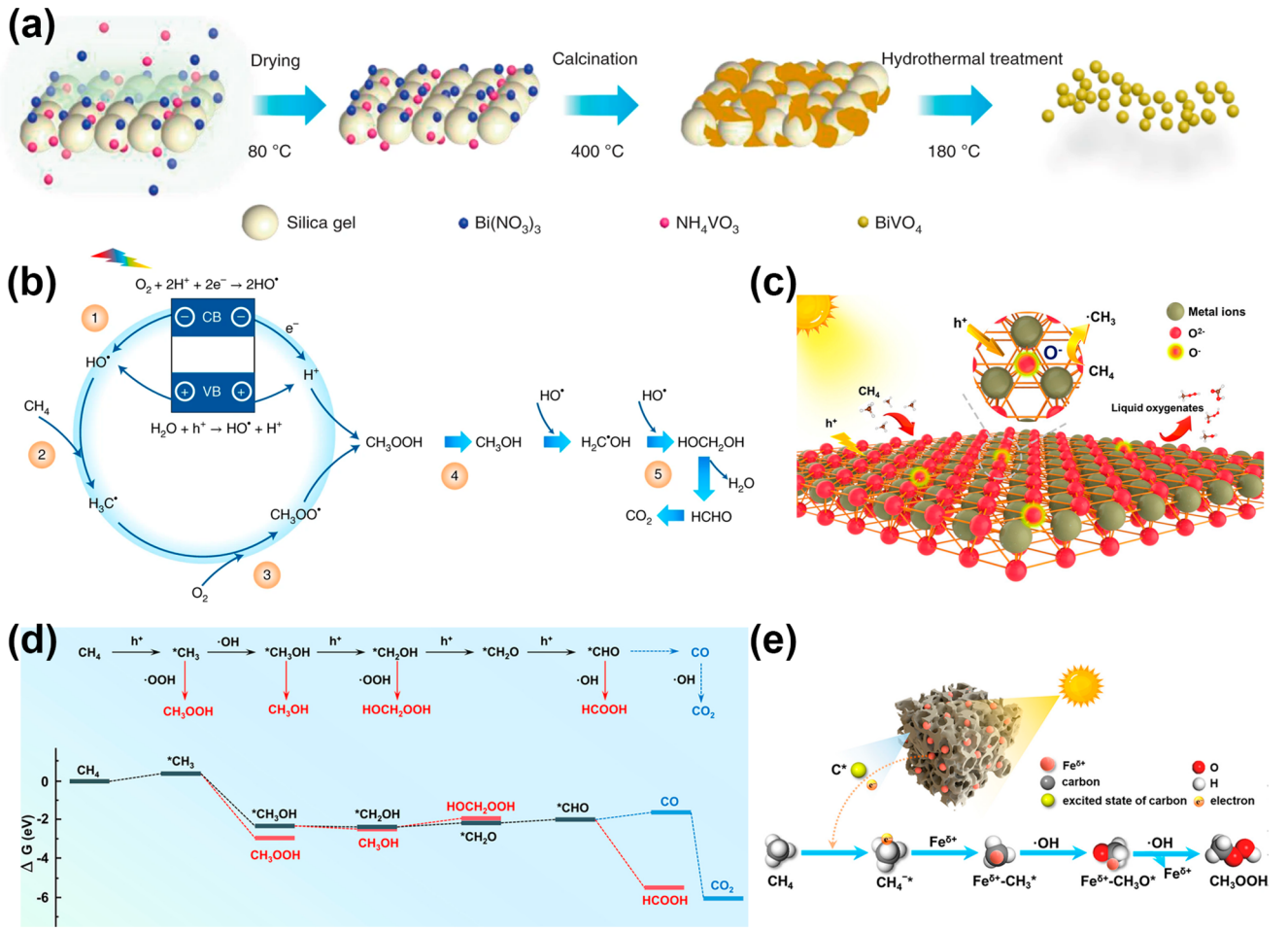

Figure 3. (a) Scheme of the synthetic route for quantum-sized $BiVO_4$. (b) Proposed reaction pathway for methane oxidation over quantum-sized $BiVO_4$. Reprinted with permission.[59] Copyright 2021, Springer Nature. (c) Schematic illustration for photocatalytic methane oxidation over ZnO nanosheets. (d) Possible reaction pathways of photocatalytic conversion of CH_4 to CH_3OH, CH_3OOH, $HOCH_2OOH$, and HCOOH over ZnO nanosheets. Reprinted with permission.[31] Copyright 2021, American Chemical Society. (e) Partial photooxidation of methane over FeCA catalyst. Reprinted with permission.[73] Copyright 2021, American Chemical Society.

chemical reactions. As for conversion systems involving oxygen, the CB of the semiconductor is required to be more negative than the electrochemical potential of $O_2/{}^{\bullet}O_2^-$ (E° = −0.33 V vs NHE, normal hydrogen electrode) or $O_2/{}^{\bullet}OOH$ (E° = −0.05 V vs NHE) to generate active radicals. ZnO[44,49,50] and TiO_2[51] are both good alternatives for the aerobic conversion of methane. For conversion systems without oxygen, the C−H bond of methane can be activated only by h^+ or •OH attacking. Therefore, the VB should be more positive than the electrochemical potential of methane oxidation ($CH_4/{}^{\bullet}CH_3$, E° = 0.83 V vs NHE) or water oxidation ($H_2O/{}^{\bullet}OH$, E° = 2.30 V vs NHE). ZnO,[30,31] TiO_2,[51] WO_3,[52] and $BiVO_4$[53−55] are all considered as appropriate semiconductors to achieve methane conversion in these anaerobic conversion systems. Nevertheless, the pure semiconductor is limited by the rapid recombination of photogenerated carriers and deficient active sites. Several strategies have been proposed in recent years such as morphology control, heteroatom doping, facet engineering, and cocatalyst modification. An elaboration on these strategies will be provided in the following sections.

3.1.1. Morphology Control. Depending on their dimensionalities, semiconductors can be classified into zero-dimensional (0D), one-dimensional (1D), two-dimensional (2D), and three-dimensional (3D) nanostructures. These materials with unique nanostructures have attracted a lot of attention owing to their size effect (0D quantum dots), large specific surface area (2D nanosheets), and effective light utilization (3D porous materials).[56,57] In this part, a detailed description about the relationship between the morphologies and photocatalytic performance can be found below.

In recent years, 0D materials such as quantum-sized semiconductors have emerged as promising photocatalysts owing to their large specific surface area, low cost, short carrier transmission path, and easy surface functionalization. The specific surface area will increase by 10^6 times when the size is reduced from a millimeter to 5 nm.[58] Under such circumstances, the performance of quantum-sized $BiVO_4$ nanoparticles (q-$BiVO_4$, 4.5 nm) for photocatalytic methane conversion was investigated by Tang's group (Figure 3a).[59] Compared with bulk $BiVO_4$, the product yield (CH_3OH and HCHO) of q-$BiVO_4$ displayed a 4-fold enhancement owing to the enhanced surface area and kinetic energy. Despite the small size of the catalyst, the morphologies, chemical states, and initial activity remained almost unchanged after 5 photocatalytic cycles (3 h per cycle). As •OH was responsible for the activation of CH_4 and the further oxidation of CH_3OH (Figure 3b), regulating the wavelength of the light source was shown to

https://doi.org/10.1021/acsenvironau.3c00002
ACS Environ. Au 2023, 3, 252−276

be an effective method to alter the •OH concentration and product selectivity. Specifically, the reaction provided a selectivity of 96.6% for CH_3OH under visible-light irradiation (400−780 nm, 170 mW cm^{-2}, 7 h), while a high HCHO selectivity of 86.7% was achieved under ultraviolet irradiation (300−400 nm, 170 mW cm^{-2}, 3 h) owing to the enhanced oxidation of CH_3OH.

0D semiconductors can be easily assembled with other components to form complex structures, such as core−shell structures and heterojunctions, which can further improve charge separation efficiency, improve stability, and modulate the active center for methane conversion. However, bulk recombination is likely to occur when the size is comparable to the width of the depletion layer.[60] Therefore, the size of the 0D semiconductor is required to be well-controlled.

2D materials such as graphene oxide (GO), graphitic carbon nitride (g-C_3N_4), and metal oxide nanosheets have gained increasing attention since the discovery of monolayered graphene.[61,62] 2D nanosheets can provide more active sites for adsorption and activation of reactants due to the large surface area. Besides, the diffusion distance for photoinduced electrons and holes to the catalyst surface is minimized owing to the atomic thickness, suppressing bulk electron−hole recombination rate and improving photocatalytic efficiency.[63,64] Graphitic carbon nitride (g-C_3N_4), a low cost and metal-free material, is considered as an attractive visible-light-responsive photocatalyst owing to its moderate bandgap (2.7 eV). The photogenerated electrons on its CB position (−1.1 eV vs NHE) can reduce O_2 or H_2O_2 to generate •OH ($H_2O_2 + H^+ + e^- \rightarrow {}^\bullet OH + H_2O$, $H_2O_2/{}^\bullet OH$ = 1.07 V vs NHE), realizing the activation of methane.[65] A 2D mesoporous g-C_3N_4 nanosheet was fabricated by polymerization of urea at 150 °C for 1 h and 550 °C for 4 h, which can disperse well in water to contact with methane molecules.[66] In the presence of H_2O_2 as the •OH source, the CH_3OH production rate is 140 μmol g^{-1} h^{-1} with 30 bar CH_4. ZnO nanosheets with a thickness of 1.53 nm were synthesized to catalyze methane oxidation at ambient temperature and pressure.[31] The formed O^- species from surface lattice oxygen can directly cleave the C−H bond in CH_4 based on experimental results (Figure 3c). Therefore, the formation rate of liquid oxygenates (CH_3OOH, CH_3OH, $HOCH_2OOH$, and HCOOH) from ZnO nanosheets was 24 times higher than that of commercial ZnO due to more surface lattice oxygen sites in the ZnO nanosheets. With the aid of H_2O_2, $^\bullet CH_3$ can react with •OH (from H_2O and H_2O_2) and •OOH (from H_2O_2) to yield CH_3OH and CH_3OOH, respectively. Afterward, the formed CH_3OH may be further oxidized to $OHCH_2OOH$ (Figure 3d). ZnO nanosheets showed a low selectivity for individual products, although the overall selectivity for liquid oxygenates can reach 90.7%. The selectivity of individual products can be improved by the rational design of the photocatalysts. In order to improve the selectivity toward CH_3OH, a unique 2D in-plane Z-scheme heterostructure was constructed between ZnO nanosheets and Fe_2O_3.[30] The Fe sites were proven to be the key active sites for improving CH_3OH selectivity. In detail, CH_4 molecules were adsorbed and polarized on the charge-accumulated Fe sites over ZnO/Fe_2O_3, accompanied by the formation of Fe−CH_3. Fe−$OHCH_3$ intermediates were then generated through the interaction between Fe−CH_3 and •OH. The electron transfer from charge-enriched Fe sites to the O atoms strengthened the polarity of the O−H bond in CH_3OH, suppressing the cleavage of the O−H bond and overoxidation of CH_3OH. For pure ZnO nanosheets, Fe−OCH_3 intermediates were more easily generated due to the relatively weak O−H bond, which can further interact with •OH and yield a series of byproducts (CH_3OOH, HCHO, HCOOH, and CO_x). Consequently, the selectivity toward CH_3OH increased from 57.1% to 99.6% after the incorporation with Fe_2O_3.

Despite the recent progress of 2D semiconductors toward photocatalytic methane conversion, the application of ultrathin 2D semiconductors is still a great challenge, especially the synthesis techniques on a large scale for potential application.[67] Besides, 2D nanosheets are easy to aggregate, resulting in the decrease of specific surface area and deterioration of performance. Moreover, various kinds of surface defects can be easily created during the synthesis of 2D nanosheets due to their atomic thickness and high specific surface area, which have a complex effect on the photocatalytic performance, related to the type, concentration, and spatial distribution of surface defects.[68] Therefore, the modulation of defects and the effect of defects on the performance of photocatalytic methane conversion should be considered in the future. It is worth noting that the refractive index of 2D semiconductors is low, which prevents them from effectively scattering incident light, thereby reducing the light utilization of the overall system.

Compared with 0D and 2D semiconductors, 3D hierarchically porous semiconductors are considered as more efficient light harvesters because the ordered macrochannels allow deep light penetration and enhanced light scattering as well as light reflection, resulting in a higher utilization efficiency.[69] Besides, the reactants can be well-confined within the pores of 3D porous semiconductors, allowing full contact with active sites. The micro (<2 nm) and meso (2−50 nm) pores contribute to the large surface area for cocatalysts modification, while macro pores (>50 nm) can facilitate the diffusion of reactants and products and thus boost the mass transport.[70] By using mesoporous KIT-6 silica as the template, 3D mesoporous WO_3 with ordered pores and specific surface area of 151 m^2 g^{-1} was prepared by a nanocasting procedure.[52] With the aid of 1 mM Fe^{3+}, the yield of CH_3OH can reach 67.5 μmol g^{-1} h^{-1} at atmospheric pressure. The performance increased by 3.4-fold compared with commercial WO_3, indicating the importance of the mesoporous structure. Similarly, a hierarchical macro-mesoporous TiO_2−SiO_2 microarray was synthesized by using polystyrenes and Pluronic triblock copolymer P123 as templates to generate macropores and mesopores, respectively.[71] Compared with the hierarchical photocatalysts, the TiO_2−SiO_2 microarray with only mesopores or macropores showed a lower methane conversion activity, demonstrating the importance of interconnected hierarchical pores. Apart from these traditional semiconductors, 3D porous carbon aerogel emerges as a star material for photocatalytic reactions owing to its low cost and high electrical conductivity.[72] Xie's group fabricated Fe clusters anchored on carbon aerogel (FeCA) via a facile sol−gel method (Figure 3e).[73] With the confinement of the carbon aerogel to Fe clusters, the performance and morphology of the photocatalyst were still retained even after 12 h of light illumination. According to X-ray photoelectron spectra (XPS) results, iron clusters were shown to exist as $Fe^{\delta+}$ ($0 < \delta \leq 3$), which could donate electrons to C* (photoexcited-state carbon atoms in carbon aerogel) to produce C^{*-}. Afterward, the electron transfer from C^{*-} to CH_4 enabled the generation of CH_4^- and $Fe^{\delta+}$−CH_3* intermediates. In the presence of H_2O_2, $Fe^{\delta+}$−CH_3* can react

https://doi.org/10.1021/acsenvironau.3c00002
ACS Environ. Au 2023, 3, 252−276

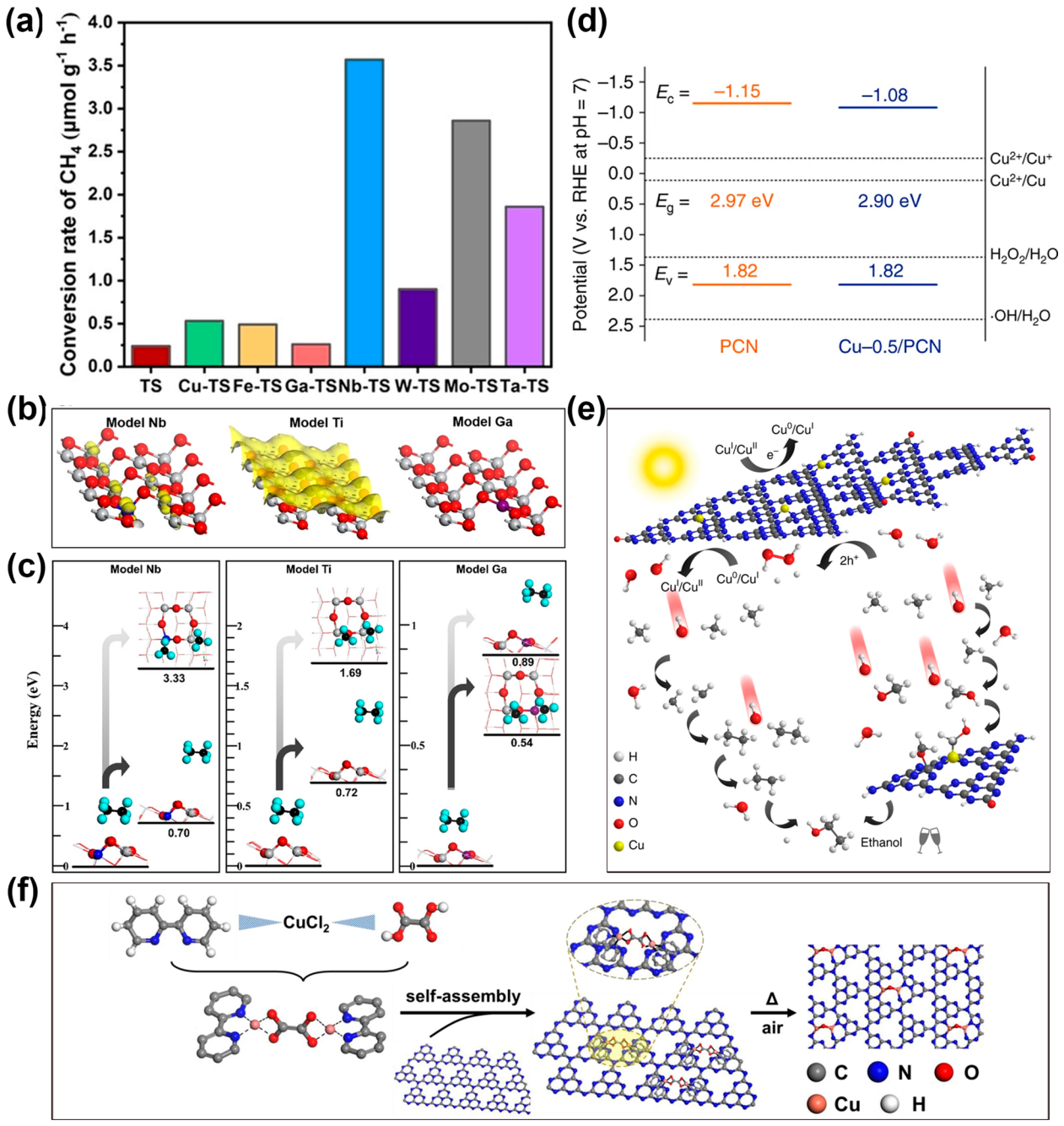

Figure 4. (a) The methane conversion rate over different metal-doped catalysts. (b) Polaron analysis of Nb-doped TiO_2, pristine TiO_2, and Ga-doped TiO_2. Ti, O, Nb, and Ga atoms are shown in gray, red, navy blue, and purple, respectively. (c) Reaction energy profiles of two competition paths of ethane desorption and C−C cleavage on Nb-doped TiO_2, pristine TiO_2, and Ga-doped TiO_2. Ti, O, Nb, Ga, C, and H atoms are shown in gray, red, navy blue, purple, black, and light blue colors, respectively. Reprinted with permission.[71] Copyright 2021, Wiley-VCH. (d) Band structure alignments of PCN and Cu-0.5/PCN. (e) The hypothetical reaction mechanism for photocatalytic methane conversion over Cu-0.5/PCN. Reprinted with permission under a creative commons CC BY 4.0.[85] Copyright 2019, Springer Nature. (f) Scheme illustration of a synthetic route for the Cu_2@g-C_3N_4 catalyst. Reprinted with permission under a creative commons CC BY 4.0.[88] Copyright 2022, Springer Nature.

with photogenerated •OH to produce $Fe^{\delta+}-CH_3O^*$ and CH_3OOH in sequence. The selectivity of CH_3OOH was strongly influenced by the concentration of H_2O_2. By optimizing the amount of H_2O_2 to 2 mmol, the selectivity and yield of CH_3OOH can be up to 100% and 13.2 mmol g_{Fe}^{-1} h^{-1}, respectively.

For 3D semiconductors, the synthesis procedure usually involves the utilization and removal of templates, limiting their extendibility and cost-effectiveness. Therefore, exploring facile template-free approaches should receive extensive attention in the future. Based on the unique advantages of 0D/2D/3D semiconductors, it may be a great idea to couple materials with different dimensions, which can further improve the activity and stability. Moreover, novel 3D materials such as hydrogels, foams, aerogels, and sponges can be considered in the field of photocatalytic methane conversion, which possess properties, of low density, stable mechanical properties, and large surface area.

3.1.2. Heteroatom Doping. Low photoinduced carrier separation efficiency is one of the most important factors

https://doi.org/10.1021/acsenvironau.3c00002
ACS Environ. Au 2023, 3, 252−276

limiting photocatalytic methane conversion.[74] Impurity doping can introduce an additional band between CB and VB, which is capable of trapping excitons and suppressing recombination of carriers in the bulk of the semiconductor. Meanwhile, impurity doping can also modulate the barrier height at the semiconductor electrolyte interface, which is beneficial for the selective charge transfer of photogenerated carriers.[75−77] For instance, the introduction of a trace amount of Si into GaN was evidenced to promote the photogenerated carrier separation efficiency according to photoluminescence (PL) spectra.[78] Furthermore, dopants can affect the surface affinity for chemical species, thus influencing the conversion efficiency of methane. Villa et al. provided a detailed explanation about the role of La dopant in methane conversion.[79] The La doping improved the specific surface area and pore volume, leading to a high adsorption ability of methane. Meanwhile, oxygen vacancies can be created after the incorporation of La, leading to a higher amount of adsorbed water compared with pure WO_3. Consequently, the CH_3OH selectivity of La-doped WO_3 increased by 50% compared with pure WO_3 because more $^{\bullet}OH$ radicals were available to react with CH_4 on the surface of La-doped WO_3.

Doping can be classified as p- and n-type doping according to the type of dopants used. The n-type-doped semiconductors and p-type-doped semiconductors can be obtained by substituting host atoms with electron-rich and electron deficient substitutes, respectively. The effects of these two different types of dopants in TiO_2 on photocatalytic methane conversion have been investigated by Zhang's group.[71] They synthesized a series of n-type (Nb, Mo, W, Ta) and p-type (Ga, Cu, Fe) doped TiO_2, which were used for nonoxidative coupling of methane. TiO_2 with n-type dopant showed a higher methane conversion rate compared with that of p-type doping TiO_2 (Figure 4a). As revealed by DFT calculations, the n-type dopants can offer excess electrons to the adjacent Ti_{6c} and Ti_{5c} atoms of TiO_2, facilitating the polarization and activation of methane molecules by transferring electrons to methane (Figure 4b). More importantly, C−C bond cleavage was more thermodynamically favorable than desorption for p-type-doped TiO_2, hindering the adsorption of new methane at the active sites and resulting in a low methane conversion rate. On the contrary, C_2H_6 tended to desorb from the surface of n-type-doped TiO_2 instead of undergoing a C−C cleavage reaction, leading to a high C_2H_6 generation rate (Figure 4c).

C_3N_4 is considered as a potential support to anchor transition metal atoms through abundant nitrogen sites. It has been demonstrated that Ni, Fe, and Cu atoms can coordinate with N atoms on the C_3N_4 framework.[80,81] Meanwhile, the fabrication procedures of doped C_3N_4 are particularly simple. Li et al. prepared a series of Zn-doped C_3N_4 photocatalysts via directly heating urea with different ratios of zinc acetate.[82] The increased binding energy of N 1s revealed by XPS indicated the formation of Zn−N bonds, which were conducive to the rapid electron transfer to a Ru cocatalyst. After doping P atoms into C_3N_4, the light absorption range was extended to 650 nm, and thus the catalysts can achieve methane conversion even under the light irradiation with a wavelength larger than 420 nm.[83] Unlike $BiVO_4$ and WO_3, the VB position of C_3N_4 is more negative than the electrochemical potential of $H_2O/^{\bullet}OH$ but more positive than H_2O/H_2O_2, which means that the holes of C_3N_4 could oxidize H_2O to H_2O_2 through a $2e^-$ pathway rather than directly to $^{\bullet}OH$. As $^{\bullet}OH$ radicals are responsible for the activation of CH_4, H_2O_2 is often required as an oxidant to generate $^{\bullet}OH$. However, the high cost of H_2O_2 holds back their industrial application.[84] Based on this, in situ generation and decomposition of H_2O_2 was achieved by introducing Cu atoms into g-C_3N_4 (Figure 4d).[85] The decomposition of the generated H_2O_2 can be achieved by mixed-valence Cu species, generating $^{\bullet}OH$ species and initiating the C−H cleavage of methane (Figure 4e). Meanwhile, the photogenerated electrons in the CB of g-C_3N_4 can reduce the oxidized Cu species to keep the initial states. It is interesting to note that the Cu-doped g-C_3N_4 showed a higher selectivity toward CH_3CH_2OH rather than CH_3OH, which can be attributed to the synergistic effect between Cu atoms and adjacent C atoms in g-C_3N_4.

In biological systems, methanotrophic bacteria can convert methane to methanol under aerobic conditions using methane monooxygenase (MMO) as catalysts. The dicopper sites in the membrane-bound MMO, one form of MMO, were demonstrated as the active sites for this transformation process.[86,87] Although the mechanism is still unclear, the performance of methane conversion reaction over diatomic Cu-doped semiconductors has been investigated by researchers. Wang's group prepared dimeric Cu-doped g-C_3N_4 (Cu_2@g-C_3N_4) as efficient catalysts for photocatalytic methane oxidation with O_2, in which every two Cu atoms were bridged by an O atom (Figure 4f).[88] The barriers required for the generation of $^{\bullet}OOH$ and $^{\bullet}OH$ from O_2 over Cu_2@g-C_3N_4 were lower than those for the single-atom Cu-doped g-C_3N_4 according to the DFT calculations, explaining the enhanced reactivity for methane conversion over the Cu_2@g-C_3N_4 catalyst.

Notably, the dopants may interact with the components in the photocatalytic system and fall off the catalyst surface, affecting the long-term stability of the photocatalyst. Therefore, we need to focus on the stability of heteroatom-doped photocatalysts in the following work. Besides, the doping amount is also an extremely vital factor to improve the performance of photocatalytic methane conversion because the excess dopants can act as the new recombination sites of photoexcited carriers. In the future, the construction of N, F, Cl, and S-doped semiconductors for the synthesis of amines, alkyl halides, and mercaptans is a direction worthy of our attention.

3.1.3. Facet Engineering. The diversity of of semiconductor facets has a great impact on the catalytic activity as well as selectivity.[76,89] The exposed surface facets may affect the photocatalytic performance through different mechanisms. For example, the adsorption and activation energy required for reactants may be varying on facets with different surface atomic arrangements.[90] Taking anatase TiO_2 as an example, the (001) facet has been verified to be more active than the (101) facet. This is because (001) facet possesses high-density, low-coordinated Ti atoms and active O atoms with a large Ti−O−Ti bond angle, which are conducive to the adsorption and activation of reactant molecules.[91]

In the field of photocatalytic methane conversion, constructing catalysts with a high percentage of active exposed facets can improve methane conversion efficiency by facilitating the adsorption and activation of methane, which is widely regarded as the rate-limiting step of the methane conversion reaction.[38] Compared with GaN thin films, GaN wires were found to exhibit a higher activity for photocatalytic methane dehydroaromatization.[78] The excellent performance of GaN wires was strongly attributed to the high proportion of

https://doi.org/10.1021/acsenvironau.3c00002
ACS Environ. Au 2023, 3, 252−276

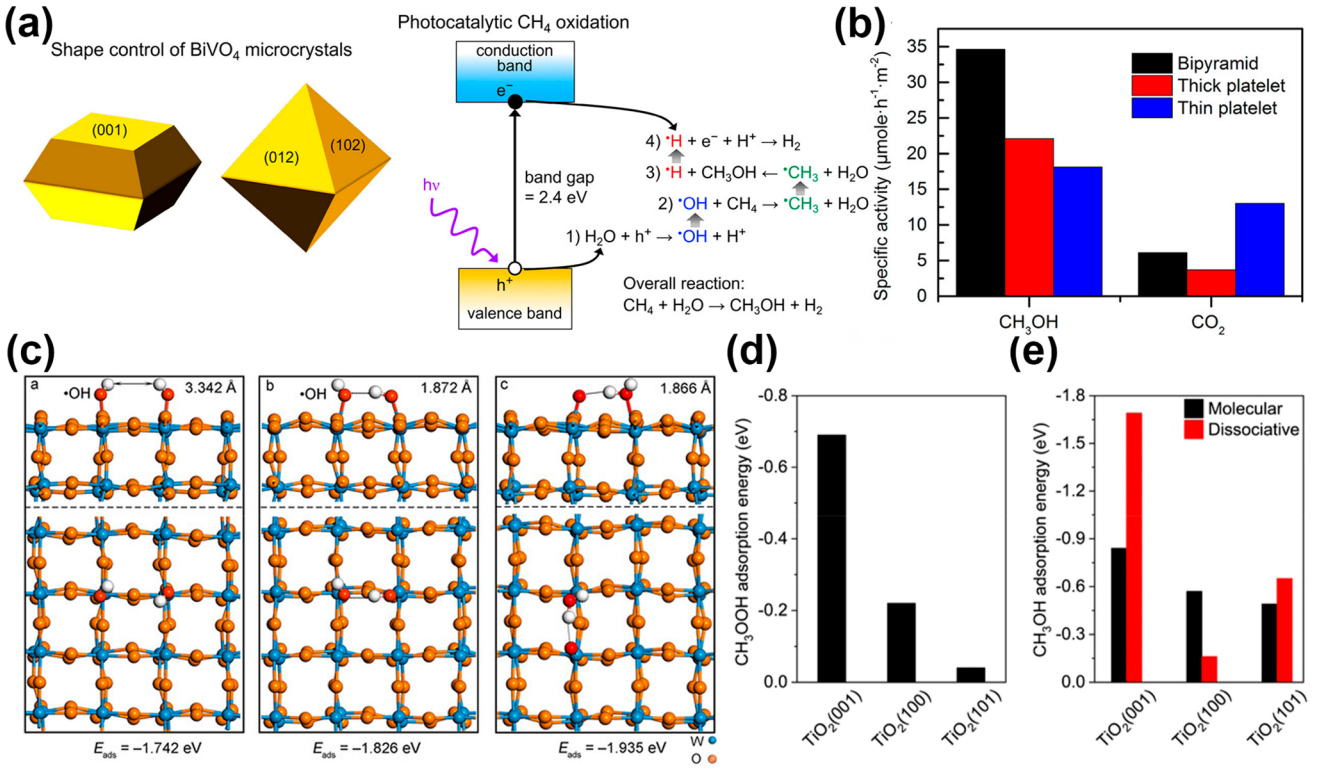

Figure 5. (a) Shape control of $BiVO_4$ microcrystals, including platelets and bipyramidal. (b) Specific activity for the conversion of CH_4 to CH_3OH over different $BiVO_4$ microcrystals. Reprinted with permission.[55] Copyright 2018, American Chemical Society. (c) The atomic structures and adsorption energy of •OH on W atoms with the (010) facet (left), (100) facet (middle), and (001) facet (right). Reprinted with permission.[100] Copyright 2021, Wiley-VCH. (d) CH_3COOH and (e) molecular and dissociative CH_3OH adsorption on TiO_2 (001), (100), and (101) surfaces. Reprinted with permission under a creative commons CC BY 4.0.[101] Copyright 2022, Springer Nature.

the m-plane (97%), which was composed of Ga and N atoms coordinated with each other. As a result, the m-plane can induce strong polarization and stretch the C−H bond of methane owing to the longer length of the Ga−N bond than the C−H bond (1.95 Å vs 1.09 Å). In contrast, the GaN thin films, containing a c-plane with only Ga atoms or N atoms, had negligible effect on the activation of methane, demonstrating the activation of the C−H bond of methane is surface-sensitive. A similar conclusion was further investigated by Yi's group.[92] They observed that ZnO nanosheets with a higher ratio of (0001) facets exhibited a faster methane conversion rate, in comparison with ZnO nanorods. The exposed polar facets were demonstrated to be more conducive to inducing polarization of highly stable molecules such as methane.

Facet engineering also has a great influence on the efficiency of charge separation and transfer.[93−95] The internal electric fields induced by polar facets may affect the migration of photoexcited electrons and holes.[92,96,97] For example, the photogenerated holes of *m*$BiVO_4$ (monoclinic scheelite bismuth vanadate) tend to transfer to (110) facets for oxidation reactions while the photogenerated electrons are accumulated on (010) facets to participate in reduction reactions.[89,98] As a result, the combination of (110) and (010) facets can lead to more efficient carrier separation and enhanced photocatalytic performance. Zhu et al. compared the performance of photocatalytic methane conversion over $BiVO_4$ with three different morphologies, including bipyramidal $BiVO_4$, thick platelet $BiVO_4$, as well as thin platelet $BiVO_4$ (Figure 5a).[55] The bipyramidal crystals possess (102) and (012) facets, while the thick and thin platelet crystals are composed of (001) facets as their top and bottom surfaces. For platelet $BiVO_4$, the photogenerated electrons are abundant on the (001) facets while holes are extracted around the perimeter. For bipyramidal $BiVO_4$, the photogenerated electrons are extracted at the apexes, while holes are abundant on the (102) and (012) facets. The highest oxidation turnover number but lowest CH_3OH selectivity were achieved over thin platelets due to the short carrier diffusion length and highly reactive rough perimeter. Bipyramidal $BiVO_4$ gave the highest CH_3OH yield and selectivity owing to its large surface area for holes and intermediate surface reactivity compared with thick and thin platelets (Figure 5b).

In addition to the conversion efficiency, facet engineering can also influence the selectivity of products by affecting the concentration and reactivity of •OHs. This is because •OHs can not only activate methane,[99] but also further oxidize CH_3OH to form CO and CO_2.[38,54] Recently, Ma et al. demonstrated that the reactivity of •OH can be tuned by controlling the facet ratios of WO_3 (Figure 5c).[100] According to the DFT calculations, the adsorbed •OH was spatially close on the (100) and (001) facet, spontaneously forming surface-bound O and H_2O. As a result, the reactivity of •OH on these two facets were diluted, while the reactivity of •OH could be maintained on (010) facet due to the extensive distance between two adjacent •OH. Therefore, facet engineering may be an effective method to transform methane into an ideal product. However, none of the above work considered the effect of facets on the adsorption and desorption ability of intermediates, which was demonstrated to play an important role in determining the selectivity in recent work (Figure 5d−

https://doi.org/10.1021/acsenvironau.3c00002
ACS Environ. Au 2023, 3, 252−276

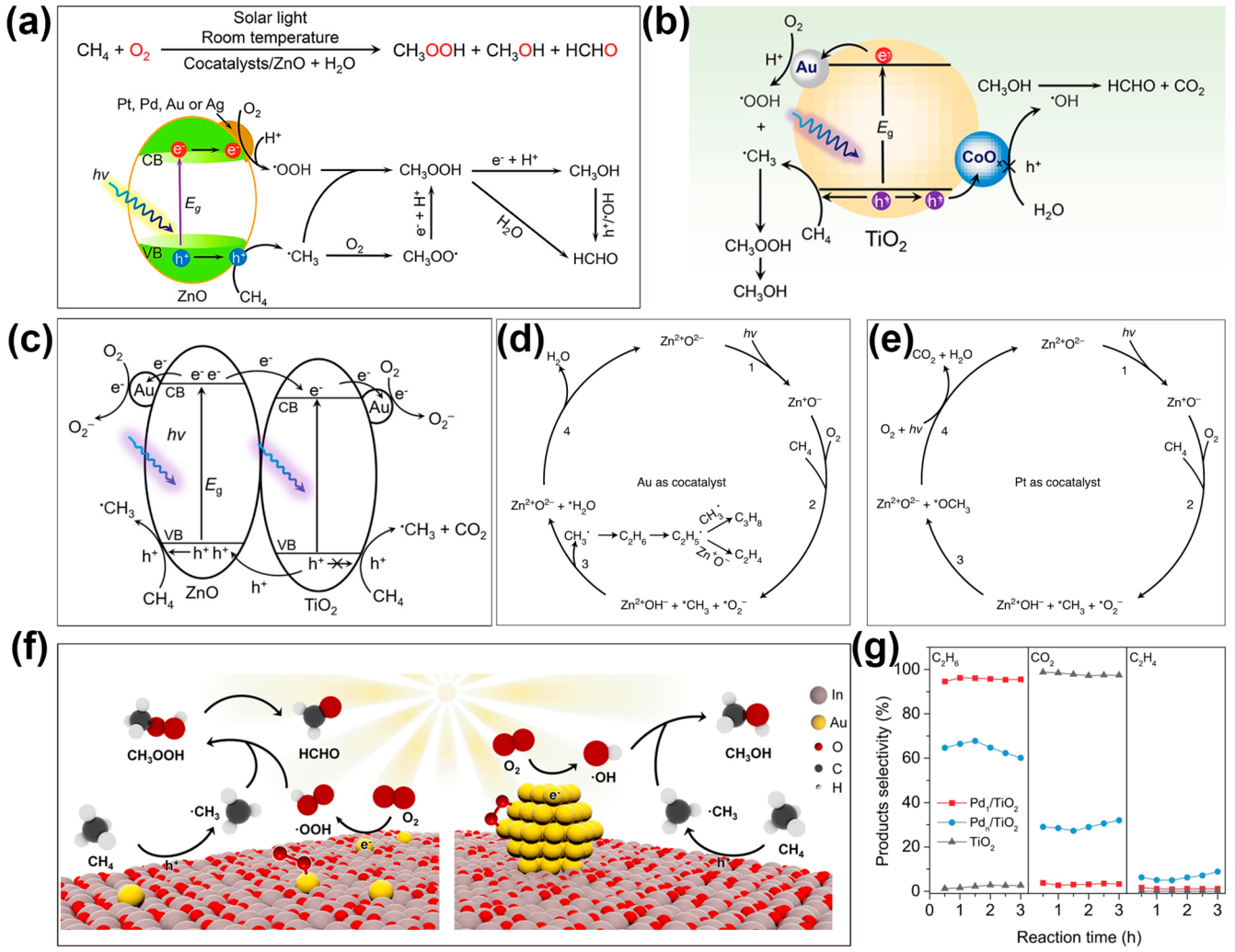

Figure 6. (a) Proposed mechanism for photocatalytic methane conversion over ZnO loaded with different cocatalysts. Reprinted with permission.[44] Copyright 2019, American Chemical Society. (b) Reaction mechanism for photocatalytic methane oxidation over Au-CoO_x/TiO_2. Reprinted with permission.[51] Copyright 2020, American Chemical Society. (c) Schematic diagram illustrating the photogenerated charge transfer process over Au-ZnO/TiO_2. (d) Reaction process on ZnO loaded with Au cocatalyst and (e) on ZnO loaded with a Pt cocatalyst. Reprinted with permission.[105] Copyright 2021, Springer Nature. (f) Proposed mechanism of photocatalytic conversion of CH_4 to HCHO or CH_3OH on Au_1/In_2O_3 or Au_{NPs}/In_2O_3, respectively. Reprinted with permission.[110] Copyright 2023, American Chemical Society. (g) The corresponding selectivity of C_2H_6, C_2H_4, and CO_2 over Pd_1/TiO_2, Pd_n/TiO_2, and pristine TiO_2. Reprinted with permission under a creative commons CC BY 4.0.[111] Copyright 2022, Springer Nature.

e). Specifically, the weak adsorption of CH_3OOH on the $TiO_2(101)$ surface allows a CH_3OOH selectivity of 100% over the $TiO_2(101)/C_3N_4$ catalyst, while HCOOH is the major product over the $TiO_2(001)/C_3N_4$ catalyst due to the overoxidation of CH_3OOH to CH_3OH and the preferential dissociation of CH_3OH on $TiO_2(001)$.[101] Moreover, the performance of high-index facets in the field of methane conversion also requires exploration.

Attention should be paid to the use of units when exploring the impact of crystal faces on the photocatalytic performance. Compared with μmol g^{-1} h^{-1}, μmol m^{-2} h^{-1} is a more suitable active unit. The unit μmol m^{-2} h^{-1} can reflect the surface activity of the catalyst, which is suitable for comparing the same type/composition but different morphology/structure of catalysts. Conversely, μmol g^{-1} h^{-1} reflects the intrinsic activity of the catalyst, which is independent of the morphology, structure, and dispersion of the catalyst. As a result, μmol g^{-1} h^{-1} is more suitable for comparing different types or compositions of catalysts.

3.2. Cocatalysts Modification

Combining semiconductors with appropriate cocatalysts is another promising strategy to tune and optimize the performance of photocatalytic methane conversion. The loaded cocatalysts can influence the performance via the two following aspects: (1) the cocatalysts can provide trapping sites for photoexcited electrons/holes to facilitate carrier separation and promote the solar-to-chemical conversion efficiency;[102] (2) the cocatalysts can accelerate the generation of reactive oxygen species, such as $^{\bullet}OH$, $^{\bullet}OOH$, $^{\bullet}O_2^-$, which can reduce the energy barrier of methane activation.[74,103,104] At present, the research on cocatalysts mainly focuses on noble metals (Pt, Au, Pd, Ag, Ru, etc.) and metal oxide (CuO_x, CoO_x, etc.) in the field of photocatalytic methane conversion. In this section, we will discuss the effect of cocatalysts on methane conversion.

Au is demonstrated as an effective cocatalyst to achieve the selective transformation of methane.[105,106] Lang et al. deposited various noble metals onto TiO_2 via a photo-

https://doi.org/10.1021/acsenvironau.3c00002
ACS Environ. Au 2023, 3, 252−276

deposition method and evaluated the performance for nonoxidative coupling of methane.[42] Compared with bare TiO_2, Ru/TiO_2, Pd/TiO_2, Ir/TiO_2, and Pt/TiO_2, Au/TiO_2 has obviously superior C_2H_6 yield and selectivity in gas−solid reaction systems, owing to the lowest contact resistance and easiest transfer of photoelectrons between TiO_2 and Au. DFT calculations revealed that CH_4 dissociation on the TiO_2 surface required a higher energy barrier than dissociation on the Au surface, disclosing that the Au cocatalyst is the reactive site. The photogenerated electrons accumulated on Au nanoparticles can activate adsorbed methane molecules into CH_3^- anions and H atoms. Then, CH_3^- anions reacted with holes to generate $^{\bullet}CH_3$ radicals, which could further combine with each other to form C_2H_6. In liquid−solid reaction systems, the role of cocatalysts was explored by Ye's group (Figure 6a).[44] They modified commercial ZnO with different noble metals (Pt, Pd, Au, Ag) via the $NaBH_4$ reduction method. The introduction of cocatalysts led to a pronounced increase in the amounts of $^{\bullet}CH_3$ and $^{\bullet}OOH$, which may be due to the enhanced separation efficiency of photoexcited carriers and the lowered energy barriers of the oxygen reduction reaction. The increased signals of these radicals led to an improved photocatalytic activity. With the participation of O_2, Au and Ag can selectively reduce O_2 to H_2O_2 through a $2e^-$ process, followed by the formation of CH_3OOH, while Pt and Pd were more efficient in the $4e^-$ oxygen reduction reaction to produce H_2O or CH_3OH. Therefore, the selectivity toward CH_3OOH or CH_3OH can be altered by modifying different types of cocatalysts.

To inhibit the excessive oxidation of methane to CO_2 and improve the selectivity toward high-value products, metal oxides with more negative VB have been employed as cocatalysts. For example, Tang's group modified CuO_x clusters on Pt/TiO_2 to avoid overoxidation of C_2H_6 in the presence of O_2.[107] The introduction of only Pt nanoparticles into TiO_2 led to a decrease in C_2H_6 selectivity but an increase in CO_2 selectivity, which resulted from the electron sink function of Pt, increasing available electrons for $^{\bullet}O_2^-$ formation, and strong oxidative holes of TiO_2. After CuO_x clusters were deposited onto Pt/TiO_2, some holes could migrate from TiO_2 to CuO_x clusters because the VB of CuO_x is more negative than that of TiO_2. Holes with relatively weak oxidation ability on CuO_x avoided the overoxidation of hydrocarbons and increased the selectivity of C_2H_6 and C_2H_4 by about 3-fold. In aqueous solution, excessive highly oxidative $^{\bullet}OH$ radicals from water oxidation were demonstrated as dominant species for the generation of overoxidized product (HCHO and CO_2). Therefore, controlling the concentration of $^{\bullet}OH$ radicals emerges as an effective method to improve the selectivity toward primary oxygenates, which can be realized by cocatalyst modification. By modification of CoO_x nanoclusters on Au/TiO_2, photoinduced holes can transfer from TiO_2 (3.0 V vs NHE) to CoO_x (2.4 V vs NHE). Up to 98% selectivity for primary products (CH_3OOH and CH_3OH) was achieved owing to the insufficient oxidation capacity to oxidize water to $^{\bullet}OH$s (Figure 6b).[51]

Recently, an ethane production rate of 5020 μmol g^{-1} h^{-1} with 90% selectivity was achieved by using $Au\text{-}ZnO/TiO_2$ as catalyst.[105] TiO_2 acted as a highly active semiconductor for methane photooxidation, enabling a high methane conversion rate, while ZnO could suppress the overoxidation of methane due to its more negative VB position compared with TiO_2, realizing a high selectivity toward C_2H_6 (Figure 6c). With the participation of O_2, Au nanoparticles considerably facilitated the adsorption and activation of O_2 according to the temperature-programmed desorption of O_2 (O_2-TPD) experiments, and the formed $^{\bullet}O_2^-$ contributed to methane conversion. In addition to conversion efficiency, the Au cocatalyst also had a very positive effect on the selectivity of C_2H_6. The $^*CH_3$ on Au sites preferred to desorb into the gas phase to produce $^{\bullet}CH_3$ rather than combining with *O to form $^*OCH_3$, as the formation of the latter required to overcome a higher activation barrier (Figure 6d−e). Therefore, a high selectivity of C_2H_6 rather than that of CO_2 can be achieved via the coupling of $^{\bullet}CH_3$ radicals. FeO_x species (FeOOH and Fe_2O_3) on TiO_2 can not only promote the charge separation but also lower the energy barrier for H_2O_2 reduction, which contributed to the improvement of the methane conversion rate.[108] The FeO_x species also played a key role in improving CH_3OH selectivity, leading to a high CH_3OH selectivity of 90%.

In addition to the types of cocatalysts, the sizes also play an important role in the efficiency of methane conversion. Through a photodeposition method, Ma et al. synthesized different-sized Pt-loaded Ga_2O_3 by simply regulating the amount of $H_2PtCl_6{\cdot}6H_2O$.[109] With the particle size ranging from 1.5 to 2.7 nm, the methane conversion rate showed a volcano-shaped trend, which reached the highest when the size is 1.9 nm. The corner sites of Pt nanoparticles are inferred to be the main active sites according to the normalized TOF of different geometric sites. Perversely, the performance of the $1.5\text{-}Pt/Ga_2O_3$ sample was suppressed despite its highest content of corner atoms. This is because C_2H_6 tends to be adsorbed by corner atoms, and Pt nanoparticles with 1.5 nm have the highest proportion of corner atoms, hindering the desorption of C_2H_6 from $1.5\text{-}Pt/Ga_2O_3$. Consequently, C−H cleavage and C_2H_6 desorption are both crucial factors affecting the efficiency of the methane conversion.

Notably, the cocatalyst modification strategy and doping strategy may have different effects on the catalytic performance. Recently, the catalytic behavior of Au single-atom-doped In_2O_3 (Au_1/In_2O_3) and Au-nanoparticles-loaded In_2O_3 (Au_{NPs}/In_2O_3) for methane oxidation was investigated by Tang's group.[110] A remarkable HCHO selectivity of 97.62% and HCHO yield of 1.98 mmol g^{-1} h^{-1} were achieved over Au_1/In_2O_3 catalyst, while a high CH_3OH selectivity of 89.42% and CH_3OH yield of 2.03 mmol g^{-1} h^{-1} were achieved over Au_{NPs}/In_2O_3 catalyst (Figure 6f). According to experiments and DFT calculations, the difference in selectivity is related to the adsorption configurations of O_2 on the surfaces of Au_1/In_2O_3 and Au_{NPs}/In_2O_3. The end-on configuration-adsorbed O_2 on Au_1/In_2O_3 preferred to be reduced to $^{\bullet}OOH$, which could react with $^{\bullet}CH_3$ to generate CH_3OOH, and the spontaneous decomposition of CH_3OOH led to the formation of HCHO. The side-on configuration-adsorbed O_2 on Au_{NPs}/In_2O_3 tended to be reduced to $^{\bullet}OH$, which then reacts with $^{\bullet}CH_3$ to generate CH_3OH product. Similarly, the different effects of Pd nanoparticles (Pd_n) and doped Pd single atoms (Pd_1) were investigated by Xiong's group (Figure 6g).[111] The Pd nanoparticles on TiO_2 acted as sites for electron accumulation, while Pd single atoms displayed the accumulation of holes due to the contribution of $Pd-O_4$ units to VB of TiO_2. The Pd-doped TiO_2 showed 94.3% selectivity toward C_2H_6 because $Pd-O_4$ units reduce the contribution of O 2p orbitals to VB, thus suppressing the overoxidation by lattice oxygen. In stark contrast, TiO_2 modified with Pd nanoparticles

https://doi.org/10.1021/acsenvironau.3c00002
ACS Environ. Au 2023, 3, 252−276

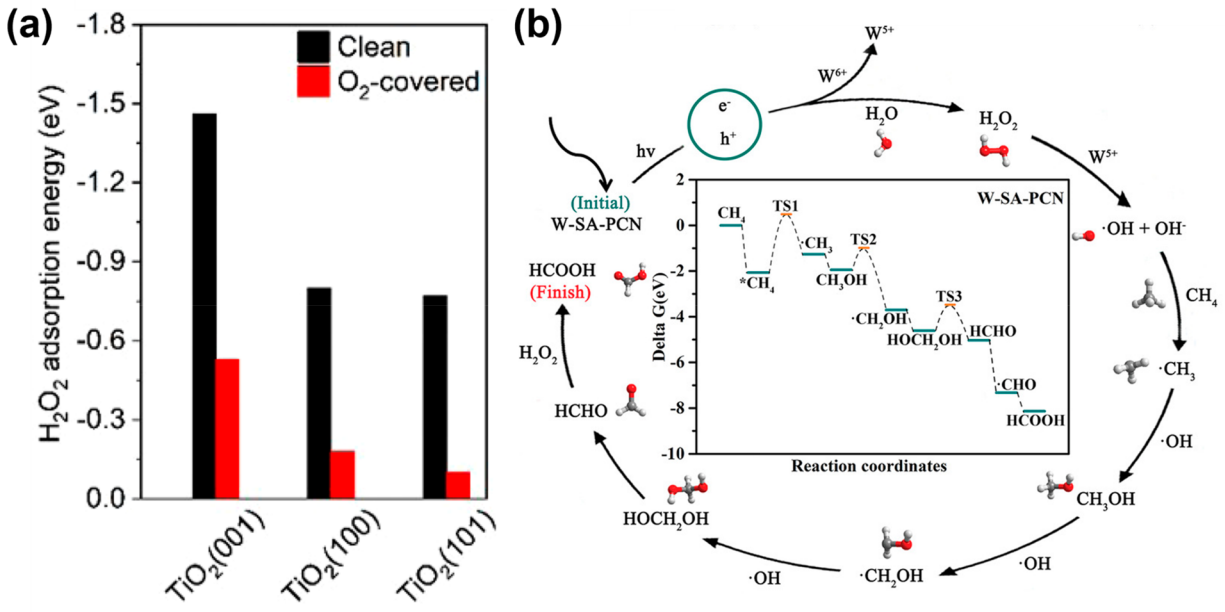

Figure 7. (a) Calculated adsorption energies of H_2O_2 on clean and O_2-covered TiO_2. Reprinted with permission under a creative commons CC BY 4.0.[101] Copyright 2022, Springer Nature. (b) Proposed reaction pathway and DFT calculations results for methane oxidation with W-SA-C_3N_4 as the photocatalyst. Reprinted with permission.[121] Copyright 2022, Wiley-VCH.

exhibited approximately 65% selectivity toward C_2H_6, as lattice oxygen played a dominant role in methane oxidation, on which the $*CH_3$ hardly desorbed to form $^{\bullet}CH_3$. Therefore, the product selectivity can be regulated by delicate design of photocatalysts.

Among noble metals, Au nanoparticles showed the highest selectivity for ethane and primary oxygenates in different systems. However, their high cost urges us to improve the atomic utilization efficiency by regulating their characteristics (such as facet, size, structure, loading amount, and surface area) or develop noble metal-free cocatalysts.

3.3. Utilization of Electron Scavengers

The addition of various of hole scavengers has been certified as an effective method to capture the holes and improve the performance of CO_2 photoreduction.[112−114] Likewise, electron scavenging agents such as MV^{2+} (methyl viologen dichloride hydrate), Fe^{3+}, Cu^{2+}, Ag^+, H_2O_2, and O_2 were revealed to have a great influence on the conversion efficiency of methane to methanol.[108]

Villa et al. gave a detailed investigation about the effect of their type and dosage on the methanol yield and selectivity.[52] The addition of electron scavengers (Fe^{3+}, Cu^{2+}, and Ag^+) not only promoted the electron−hole pair separation but also inhibited the photocorrosion of WO_3 by scavenging photogenerated electrons, leading to an enhanced total productivity (including CH_3OH, C_2H_6, and CO_2). In addition, the different electron scavengers often lead to various catalytic selectivity. The added Ag^+ resulted in the complete oxidation of methane to CO_2 because Ag^+ can be reduced to Ag by the photogenerated electrons of WO_3. In the presence of Fe^{3+} with optimized concentration (1 mM), both the generation rate and selectivity of CH_3OH can be improved. However, the addition of Fe^{3+} may bring about severe water pollution and do harm to biological health,[115−117] hindering its practical application in methane conversion.

Compared with Fe^{3+}, H_2O_2 is regarded as a clean oxidant for chemical production and environmental remediation owing to the nontoxic products (H_2O and O_2).[118] H_2O_2 can not only promote the carrier separation efficiency by scavenging photogenerated electrons, but also produce active species ($^{\bullet}OH$ and $^{\bullet}OOH$) via electrons-mediated reduction process, which can react with methane molecules to generate oxygenate products.[66,119,120] However, in addition to being reduced by photogenerated electrons into $^{\bullet}OH$ (0.06 eV vs RHE) or $^{\bullet}OOH$ (−0.38 eV vs RHE), H_2O_2 can also be oxidized into O_2 by photogenerated holes facilely, lowering the H_2O_2 use efficiency for methane conversion ($H_2O_2 + 2h^+ \rightarrow O_2 + 2H^+$).[31,66]

Considering the high cost of H_2O_2, the utilization efficiency of H_2O_2 needs to be improved. A recent work demonstrated that O_2 additive with proper concentration can lead to a high H_2O_2 use efficiency of 93.3% and enhanced methane conversion rate.[101] The added O_2 was shown to suppress H_2O_2 adsorption on photocatalysts and inhibit the decomposition of H_2O_2 to O_2 mediated by holes (Figure 7a). Whether H_2O_2 is reduced to $^{\bullet}OH$ or $^{\bullet}OOH$ depends on the catalyst used. Over TiO_2 catalysts, the $^{\bullet}OH$ radicals were obtained from H_2O_2 due to the insufficient potential of electrons on TiO_2. Over TiO_2/C_3N_4 composites, the electrons were mainly located on the CB of C_3N_4 owing to the formed Z-scheme heterojunctions, resulting in the generation of dominant $^{\bullet}OOH$ radicals. Another alternative approach is the in situ generation and decomposition of H_2O_2. For instance, Zhang's group designed W single-atom modified C_3N_4 by calcining urea and $Na_2WO_4{\cdot}2H_2O$ in the atmosphere.[121] $W^{\delta+}$ species not only acted as the active sites for methane activation but also as the center for H_2O_2 production and reduction (Figure 7b). The W modified C_3N_4 (1.6 μmol L^{-1}) catalyst exhibited a 4-fold increase in H_2O_2 production over pure PCN (0.4 μmol L^{-1}). As a result, CH_3OH yield can reach up to 215 μmol g^{-1} h^{-1} without any additional sacrificial agent, 24 times higher than that of single PCN.

https://doi.org/10.1021/acsenvironau.3c00002
ACS Environ. Au 2023, 3, 252−276

Table 1. Overview and Performance of Various Photocatalytic CH_4 Conversion Systems Using Different Regulating Strategies

Photocatalyst	Reaction Conditions: Reactants	T (°C)	Light	Reactor	CH_4 conv. (%)	Products (yields, selectivity)	ref.
Design of Semiconductors							
(1) Morphology control							
Quantum-sized $BiVO_4$	1 MPa CH_4, 1 MPa O_2, 10 mg catalyst, 10/80 mL H_2O	25	Xe lamp, 170 mW cm^{-2}, 300−400 nm	Batch reactor	−	HCHO, 1871.4 μmol g^{-1} h^{-1}, 86.7%	[59]
			Xe lamp, 170 mW cm^{-2}, 400−780 nm			CH_3OH, 366.7 μmol g^{-1} h^{-1}, 96.6%	
Mesoporous g-C_3N_4	3 MPa CH_4, 50 mM H_2O_2, 15 mg catalyst, 25 mL H_2O	35	300 W Xe lamp, AM 1.5G filter	Batch reactor	−	CH_3OH, 800 μmol g^{-1} (after 10 h)	[65]
ZnO nanosheets	0.1 MPa CH_4, 500 μL H_2O_2 (30 wt % in H_2O), 4 mg catalyst, 10 mL H_2O	50	300 W Xe lamp, AM 1.5G filter	Batch reactor	−	Methyl oxygenates (CH_3OOH, CH_3OH, $HCOOH$, $HOCH_2OOH$), 2.21 mmol g^{-1} h^{-1}, 90.7%	[31]
ZnO/Fe_2O_3 porous nanosheets	0.1 MPa CH_4, 10 mg catalyst, 5 mL H_2O	25	300 W Xe lamp, AM 1.5G filter	Batch reactor	−	CH_3OH, 118.84 μmol g^{-1} h^{-1}, 99.6%	[30]
Fe cluster/carbon aerogel	0.1 MPa CH_4, 8 mM H_2O_2, 10 mg catalyst, 9.8 mL H_2O	50	300 W Xe lamp, AM 1.5G filter	Batch reactor	−	CH_3OOH, 13.2 mmol g_{Fe}^{-1} h^{-1}, 100%	[73]
(2) Heteroatom doping							
Si-doped GaN	150 μmol CH_4, 0.35 mg catalyst	5	7.5 mW cm^{-2}, 290−380 nm	Batch reactor	−	C_6H_6, 58 μmol g^{-1} h^{-1}	[78]
La-doped WO_3	4.5 mL min^{-1} CH_4, 17.9 mL min^{-1} He, 0.3 g catalyst, 300 mL H_2O	55	Medium-pressure Hg lamp	Flow reactor	−	CH_3OH, 31.3 μmol g^{-1} h^{-1}, 47%	[79]
Nb-doped TiO_2/SiO_2	1 mL CH_4, 100 mg catalyst	25	300 W Xe lamp	Batch reactor	−	C_2H_6, 1.7 μmol g^{-1} h^{-1}, 99%	[71]
Ru/Zn-doped g-C_3N_4	0.05 MPa CH_4−CO_2−Ar mixture (molar ratio 7.5:7.5:85), 100 mg catalyst	80	150 W Xe lamp	Batch reactor	−	CH_3CHO, 130.4 μmol g^{-1} h^{-1}, 15% CH_3CH_2OH, 500.5 μmol g^{-1} h^{-1}, 57.5%	[82]
P-doped g-C_3N_4	27 mL CH_4, 3 mL O_2, 5 mg catalyst, 20 mL H_2O	25	300 W Xe lamp, 100 mW cm^{-2}	Batch reactor	−	CH_3CH_2OH, 51 μmol g^{-1} h^{-1}, 62.7%	[83]
Cu-doped g-C_3N_4	10 mL min^{-1} CH_4, 90 mL min^{-1} N_2, 20 mg catalyst, 25 mL H_2O	25	500 W Xe lamp	Flow reactor	−	C_2H_5OH, 106 μmol g^{-1} h^{-1}, 81%	[85]
Diatomic Cu-doped g-C_3N_4	1 MPa CH_4, 0.5 MPa O_2, 1.5 MPa Ar, 50 mg catalyst, 10 mL H_2O	50	300 W Xe lamp, λ > 420 nm, 100 mW cm^{-2}	Batch reactor	10.1%	Methyl oxygenates (CH_3OOH, CH_3OH), 1399.3 mmol g_{Cu}^{-1} h^{-1}, 98%	[88]
(3) Facet engineering							
$BiVO_4$ (bipyramid)	10% CH_4,	65	350 W Xe lamp	Flow reactor	−	CH_3OH, 111.9 μmol g^{-1} h^{-1}, 85.0%	[55]
$BiVO_4$ (thick platelet)	90% Ar,					CH_3OH, 79.2 μmol g^{-1} h^{-1}, 85.7%	
$BiVO_4$ (thin platelet)	0.2 g catalyst, 20 mL H_2O					CH_3OH, 65.7 μmol g^{-1} h^{-1}, 58.2%	
Cocatalysts Modification							
Au/TiO_2	10% CH_4, 90% Ar, 5 mg catalyst	−	300 W Xe lamp, AM 1.5G	Flow reactor	−	C_2H_6, 81.7 μmol g^{-1} h^{-1}, 95%	[42]
Au/ZnO	2 MPa CH_4, 0.1 MPa O_2, 10 mg catalyst, 100 mL H_2O	25	300 W Xe lamp, 100 mW cm^{-2}, 300−500 nm	Batch reactor	−	Oxygenates (CH_3OOH, HCHO, CH_3OH), 12.5 mmol g^{-1} h^{-1}, 95.4%	[44]
$Cu_{0.1}Pt_{0.5}/TiO_2$	O_2:CH_4 = 1:400, 100 mg catalyst	25	40 W LED lamp, 365 nm	Flow reactor	−	C2 (C_2H_6, C_2H_4), 68 μmol g^{-1} h^{-1}, 60%	[107]
Au-CoO_x/TiO_2	2 MPa CH_4, 0.1 MPa O_2, 10 mg catalyst, 100 mL H_2O	25	300 W Xe lamp, 450 mW cm^{-2}, 300−500 nm	Batch reactor	−	Methyl oxygenates (CH_3OOH, CH_3OH), 2540 μmol g^{-1} h^{-1}, 95%	[51]
Au-ZnO/TiO_2	air:CH_4 = 1:69, 70 mL min^{-1}, 20 mg catalyst	25	300 W Xe lamp, 500 mW cm^{-2}, 300−500 nm	Flow reactor	−	C_2H_6, 5000 μmol g^{-1} h^{-1}, 90%	[105]

https://doi.org/10.1021/acsenvironau.3c00002
ACS Environ. Au 2023, 3, 252−276

Table 1. continued

Photocatalyst	Reaction Conditions: Reactants	T (°C)	Light	Reactor	CH_4 conv. (%)	Products (yields, selectivity)	ref.
FeO_x/TiO_2	20% CH_4, 80% Ar,10 mg catalyst, 6 mL H_2O, 4 mL, 2 mM H_2O_2	25	300 W Xe lamp, λ < 710 nm	Batch reactor	15%	CH_3OH, 350 μmol g^{-1} h^{-1}, 90%	[108]
Au_{NPs}/In_2O_3	2 MPa CH_4, 1 MPa O_2,	25	250 mW cm^{-2}, 300−1100 nm	Batch reactor	–	CH_3OH, 2030 μmol g^{-1} h^{-1}, 89.42%	[110]
Au_1/In_2O_3	10 mg catalyst, 180 mL H_2O					HCHO, 1980 μmol g^{-1} h^{-1}, 97.62%	
Pd_n/TiO_2	0.1 MPa CH_4, 3 mg catalyst	25	300 W Xe lamp	Batch reactor	–	C_2H_6, 180 μmol g^{-1} h^{-1}, ~ 65%	[111]
Pd_1/TiO_2						C_2H_6, 910 μmol g^{-1} h^{-1}, 94.3%	
Utilization of Electron Scavengers							
Mesoporous WO_3	4.5 mL min^{-1} CH_4, 17.9 mL min^{-1} He, 0.3 g catalyst, 300 mL H_2O	55	Medium-pressure Hg lamp	Flow reactor	–	CH_3OH, 29.8 μmol g^{-1} h^{-1}, 46%	[52]
Mesoporous WO_3 (1 mM Fe^{3+})						CH_3OH, 67.5 μmol g^{-1} h^{-1}, 58.5%	
Mesoporous WO_3 (0.1 mM Cu^{2+})						CH_3OH, 46.8 μmol g^{-1} h^{-1}, 38.4%	
Mesoporous WO_3 (2 mM Ag^{+})						CH_3OH, 17.3 μmol g^{-1} h^{-1}, 11.8%	
TiO_2/C_3N_4	8% CH_4 + 92% Ar, 165 μL 1 M H_2O_2, 20 mg catalyst, 20 mL H_2O	25	300 W Xe lamp	Flow reactor	8.6%	HCOOH, 235 μmol g^{-1} h^{-1}, 56.4%	[101]
	8% CH_4 + 4% O_2 + 88% Ar, 165 μL 1 M H_2O_2, 20 mg catalyst, 20 mL H_2O				16.7%	HCOOH, 486 μmol g^{-1} h^{-1}, 69.8%	
W-PCN	0.5 MPa CH_4, 0.1 MPa O_2, 10 mg catalyst, 5 mL H_2O	–	300 W Xe lamp, 200 mW cm^{-2}	Batch reactor (gas−solid system)	–	CH_3OH, 215 μmol g^{-1} h^{-1}, CH_3OH/HCOOH = 80%	[121]

https://doi.org/10.1021/acsenvironau.3c00002
ACS Environ. Au 2023, 3, 252−276

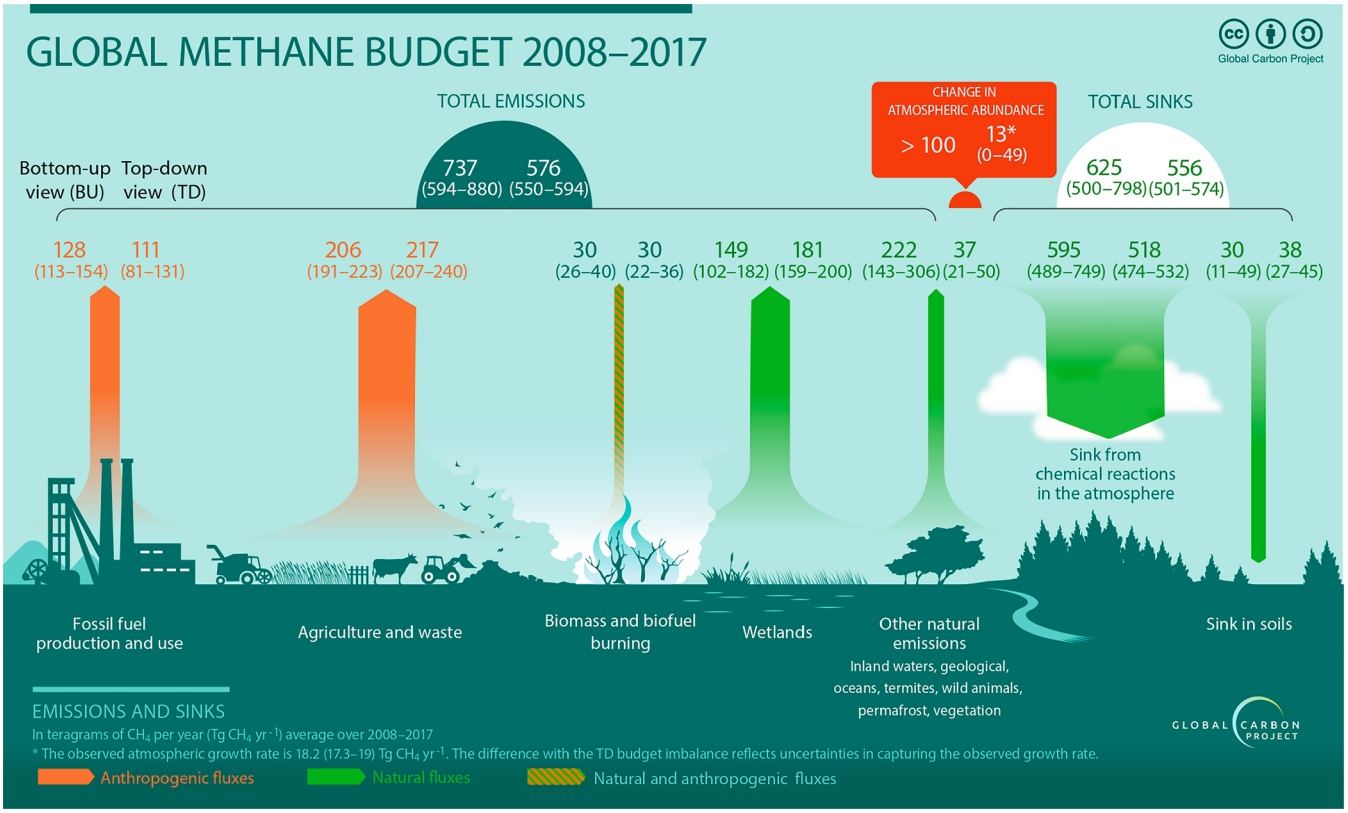

Figure 8. Global methane budget for total emissions and sinks during 2008−2017. Reprinted with permission under a creative commons CC BY SA 4.0.[122] Copyright 2020, Copernicus.

Compared with the addition of various electron scavengers, in situ generation and decomposition of H_2O_2 are green and low-cost methods to facilitate carrier separation. Meanwhile, the generated $^{\bullet}OH$ or $^{\bullet}OOH$ can promote methane conversion reactions. However, the in situ generation and decomposition of H_2O_2 are limited to C_3N_4-based photocatalysts. Future studies should consider the exploration of photocatalysts that can oxidize H_2O into H_2O_2 via a $2e^-$ pathway. Besides, the amount of H_2O_2 should be controlled because of its two sides of product selectivity.

Overall, this review presents typical engineering strategies for improving methane conversion efficiency and selectivity, including morphology control, heteroatom doping, facet engineering, cocatalyst modification, and utilization of electron scavengers. With the help of these strategies, the activity and selectivity of methane conversion can be improved through a reasonable material design. As shown in Table1, a summary of the photocatalysts used, reaction conditions, and specific data for the above photocatalytic methane conversion systems is provided.

4. APPLICATION SCENARIOS

The major sources of methane emissions and the global methane emissions and sinks are roughly shown in Figure 8.[122] Anthropogenic methane emissions on earth are estimated to be equal to natural methane emissions.[123] Here, we focus on discussing the anthropogenic methane emission scenarios because they are much easier to control and quantify than natural methane emission sources. The application scenarios for methane conversion can be broadly divided into the complete oxidation of low-level emitted sources and the resource recovery from some concentrated sources, including identification of methane emission sources, accounting of emissions at each stage, as well as available mitigation technologies. The summaries presented above of existing photocatalytic methane conversion technologies give a promising picture of efficient methane utilization and mitigation. Unfortunately, no commercialized pilot or large-scale applications of photocatalytic methane conversion have been reported. Through examples and analysis of possible photocatalytic application scenarios, combined with a literature review of potential industrial applications, we hope to provide suggestions for the sustainable development of photocatalytic methane conversion in the future.

4.1. Emitted Methane Total Oxidation for Climate Mitigation

Dilute methane emitted from scattered sources is the dominant factor influencing global warming in most scenarios. For example, methane from livestock breeding, rice cultivation, biomass burning, and coal mining accounts for 40% of anthropogenic methane emissions.[124] Besides, wetlands, with an average methane emission of 102−200 Mt yr^{-1}, are considered as the largest natural methane emitter here on the earth, accounting for about a quarter of global methane emissions.[4,125] Here, we describe low-concentration methane as atmospheric methane or higher concentrations of methane within a particular space (e.g., below 2% in vol.). Treating these low-concentration but high-volume emitters can reduce the impact of the short-term warming spike caused by methane radiative forcing and provide time for long-term greenhouse gas treatment.

Take the ventilation air in coal mines as an example of low-level methane emissions. Methane is typically less than 1 vol %

https://doi.org/10.1021/acsenvironau.3c00002
ACS Environ. Au 2023, 3, 252−276

in ventilation air but contributes about 60−70% of total CH_4 emissions from coal mining activities.[126,127] In order to avoid the direct emission of methane into the atmosphere, the enrichment of methane in ventilation air is considered as one of the effective means of mine exhaust treatment, and concentrated methane flow could be used as fuel gas of lean-burn gas turbines burning for heat and electricity generation.[128,129] Commercialized methane separation involved membrane separation and adsorption-based separation. Though membrane can purify acidic gases from methane flows, it suffers from the limitations of capital investment and replacement cost of the membrane and is not able to recovery methane from ventilation air flows.[13,129] In contrast, physical or chemical adsorption is more effective and applicable for the enrichment of methane with a lower concentration. For example, an adsorption-based separation process adopted a two-stage progressive enrichment strategy and obtained methane concentration of more than 25% as well as methane recovery of up to 99%.[130] Another typical scenario of low-concentration methane emission is the oil and natural gas industry, where most diluted methane emissions are fugitive losses from vents, leaks, and unlit flares during the production, processing, transportation, and distribution of natural gas resources.[122] For instance, Hawkes et al.[131] calculated that the major global natural gas supply chains as mentioned above could emit 26.4 Mt CH_4 into the atmosphere in 2017. Although the accounting scope and emission factors can affect the estimated results of the study, the annual growth trend of total fugitive methane emissions from natural gas is consistent.[132,133] It was reported that the mean leak concentration of a natural gas pipeline in Washington, DC was 4.6 ppm of CH_4 while the maximum reached 88.6 ppm of CH_4.[134] Available low-concentration methane abatement technologies in the natural gas industry focus on associated leak detection and remediation as well as gas recovery.[135,136] For example, Ravikumar et al. found that a leak detection and remediation process reduced total emissions by 44%, and 90% of leaking sources stopped emitting in subsequent measurements.[137] In addition, as opposed to the zero benefit of direct emissions, concentrating these relatively high concentrations of low level methane, similar to that of ventilation air in coal mines, for heat and electricity generation is technically possible.

But as a low grade energy, it is obvious that the enrichment and purification of methane in scenarios with lower concentration (i.e., as low as dozens of ppm or even atmospheric level methane) is economically unfavorable and not suitable as it is a process with huge energy consumption and little benefit.[13] For example, ruminants are the largest source of methane emissions in animal husbandry, with around 2/3 of livestock methane emissions in the European Union coming from enteric fermentation and 1/3 from manure.[138] Methane emissions from ruminants are mainly produced in the rumen and intestine through anaerobic fermentation.[139] Recently, researches focus on the front-end prevention of methane emissions from ruminants, such as dietary regulation (improved nutrition intake,[140] feed additives[141]), manure management,[142] etc., which can prevent more than 20% of ruminant methane emissions,[143,144] equivalent to at least 42 Mt yr^{-1} of methane reduction. But the rest of the largely inevitable methane emissions still pose a challenge to greenhouse gas mitigation. And the end-of-pipe treatments of discharged methane face the challenges of variability of the mixed gas components and very dilute methane concentration in air, while the expensive operation costs or temporarily insurmountable technical obstacles (e.g., enrichment and purification of methane flow) make it difficult for methane in near atmospheric level scenarios such as pasture to be recycled into flammable gases.

In addition, the conversion of low concentration methane to methanol seems to be an attractive one. Because methanol is generally a vital intermediate for further upgrading of industrial products originating from methane. Steam methane reforming is the most widely used indirect process route for methanol production nowadays due to its technological maturity and relatively low investment.[145] In the downstream industry, methanol can further produce traditional chemicals, for instance formaldehyde, acetic acid, etc., and emerging products or fuels, such as olefins, dimethyl ether, methyl *tert*-butyl ether, etc.[146] It is forecasted that the total demand of the global methanol market could reach 110 million metric tons by 2023.[147] However, even if the total methanol demand is converted to the mass of methane consumed (e.g., 220 MMT by steam methane reforming with an estimated conversion of 50%), it is not enough to reverse the trend of atmospheric methane growth or affect atmospheric methane stocks (e.g., the newly increased annual total methane emissions reached 737 million metric tons).[122] It seems that the environmental impact created by the conversion of methane to methanol is nearly negligible. Moreover, many factors restrict the further development of atmospheric methane resources. For example, the conversion process is trapped by the same premise that existing advanced purification technologies cannot support the enrichment of dilute methane to meet the industrial requirements for inhibiting the occurrence of side reactions and ensuring methanol selectivity.

Therefore, it is not appropriate to regard atmospheric level methane as a kind of resource so far. The more effective measure to get an environmental benefit from the short-term climate mitigation of methane abatement is to directly convert atmospheric methane into carbon dioxide, and it is proposed that this process will not aggravate the greenhouse effect when we talk about the global atmospheric reserves of CO_2. For example, Plata et al. proposed a low-temperature thermal catalytic method using earth-abundant copper-doped mordenite zeolite to catalyze the complete oxidation of atmospheric concentration CH_4 to CO_2, which could reduce a considerable 410 Mt Yr^{-1} of CO_2e global coal mine methane emissions.[20]

However, if existing photocatalytic technologies are applied, they also have the potential to achieve 100% conversion of atmospheric methane in a more suitable environment for catalysts. Compared to thermal catalysts, electrical catalysts, and biocatalysts, photocatalysts get distinct advantages in the treatment of low-concentration methane emissions: (1) photocatalysis has a wider operating concentration range and can maintain a high conversion efficiency at a relatively low methane concentration; (2) except for solar energy, no additional energy input is required, which will undoubtedly save the user's operating costs; (3) commercially available catalysts such as TiO_2 and ZnO are inexpensive, and the reactor structure is simple and easy to a maintenance. It is promising and ecofriendly to deploy photocatalysts in surface methane emission sources, and it is expected to make great contribution for atmospheric methane mitigation. Photocatalysts can be deployed in any scenario where adequate lighting and active ventilation can be achieved, such as

https://doi.org/10.1021/acsenvironau.3c00002
ACS Environ. Au 2023, 3, 252−276

pipelines and venting stations in the oil and gas industry. For example, CuO/ZnO[148] and Ag-ZnO[149] have been investigated for the total oxidation of methane (100−200 ppm) to CO_2 within 30 min under the simulated sun light irradiation, demonstrating that photocatalysis has the advantages of lower sensitivity to methane concentration and ambient temperature over thermal catalysis. Unfortunately, photocatalytic conversion at lower concentrations (even at atmospheric methane concentrations) has not been reported. Subsequent studies could focus on the direct photocatalytic oxidation of atmospheric methane with more climate mitigation implications.

The basic photocatalytic system generally consists of a photocatalyst, photoreactor, reaction medium, light source, and so on. Reasonable design of the photocatalytic system plays an important role in improving catalytic performance and technical competitiveness. In addition to the general strategies for enhanced light harvesting, thermal-assisted photocatalysis, and photocatalysts modifications that have been discussed in detail in previous sections, the efficient mass transfers in reactor systems are worthy of further studies. There are two major types of photoreactors for methane conversion: batch reactor and flow reactor. The batch reactors are usually purged with certain ppm methane and oxidants (e.g., O_2, H_2O_2, H_2O) after vacuuming and sealed before reaction. The flow reactors are continuously fed with mixture gases throughout the reaction process. Generally, batch reactor systems are suitable for total oxidation of methane to carbon dioxide due to a higher retention time, but the limited adsorptions of methane on the surface of the catalyst are mainly driven by the free diffusion of methane molecules. And it seems like mass transfer, rather than photocatalytic efficiency itself, determines the limited yield rate of carbon dioxide. While for flow reactor systems, although the conversion ratio of methane is reduced, the yield rate of CO_2 increases due to more evenly dispersed methane molecules by complex flow changes and more efficient methane absorption. For example, when Ag-ZnO was utilized in a batch photoreactor containing 100 ppm of methane, the methane conversion ratio reached 100%, and the calculated CO_2 yield rate was 4.8 μmol h^{-1}; however, if the catalyst was put into the flow reactor with a mixed methane/air flow rate of 25 mL min^{-1}, the methane conversion ratio slightly dropped to 98.5%, and the calculated CO_2 yield rate increased to 6.5 μmol h^{-1}, suggesting the benefits of mass transfer improvement over photocatalytic methane oxidation.[149] Of course, it does not mean the flow reactor is better than batch reactor; the adjustments of the reactor should depend on the consideration of many factors such as desired methane conversion effect, economic issue, light energy input, etc.

In addition to the above lab-scale advances, the solar chimney power plant (SCPP) coupled with photocatalytic reactors was proposed for continuous large-scale atmospheric level methane removal, where the whole system consists mainly of four parts: heat collector, catalyst bed, turbine, and chimney, as depicted in Figure 9.[150] The principles of SCPP are as follows: (1) the air is heated by solar light in a heat collector to form the updraft; (2) CH_4 is oxidized to CO_2 and water vapor as the air flows through the photocatalyst bed; and (3) the powerful flow created by the stack effect then spins the turbine to generate electricity. Subsequently, Ming et al. developed a numerical model to evaluate the photocatalytic methane removal efficiency and electricity generation performance.[151] Interestingly, they found that nearly 30.6 kg of

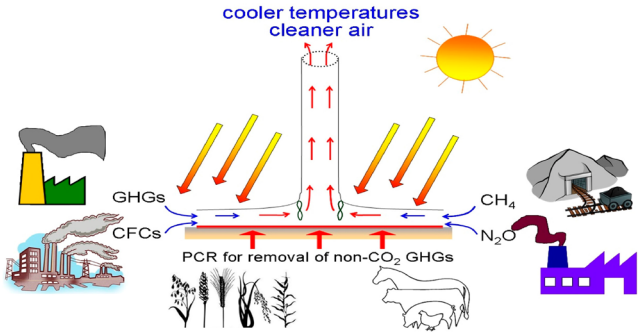

Figure 9. Combined solar chimney power plant and photocatalytic reactors for non-CO_2 greenhouse gas removal. Reprinted with permission under a creative commons CC BY 4.0.[150] Copyright 2017, Elsevier.

atmospheric methane could be degraded during the daytime with a maximum photocatalytic efficiency of up to 96.5% and an average turbine output power reached 17.04 kW in an hour (with an average air volume flow rate of 688 m^3 s^{-1} and corresponding atmospheric methane purification rate of 0.7 g s^{-1}).[151]

Although the construction costs and footprint are still the main limitations of SCPP, direct atmospheric methane treatment should focus on the improvement of reactor system design, as discussed above. Meanwhile, the operational stability, engineering applicability, and environmental impact assessments are also critical links to these photocatalytic systems. Due to the high uncertainty of economic and environmental feasibility in methane treatment, it is suggested that any emerging technologies should weigh their own life cycle assessment (LCA) costs against the potential climate benefits. Very recently, a prospective LCA of photocatalytic methane total oxidation to CO_2 was proposed, claiming that a self-sufficient photocatalytic module can amortize the produced GHG emissions within 1.5 years under the best-case scenario in 2050, and the future feasibility of this system is investigated.[152] Through LCA analyses, this limited but prospective work provides guidance for the future development of photocatalytic low concentration methane oxidation researches.

4.2. Concentrated Methane for Chemical Production

It should be noted that the concentration of most methane emitted into the atmosphere is barely impossible for enrichment or recycling due to the unfavorable considerations of undeveloped enrichment technologies, capital investment, operation cost, etc. And currently catalytic methane conversions require high concentration or even pure methane to ensure the well production of higher hydrocarbon products under existing industrial production systems and the methanol market. Therefore, in this part, we focus on concentrated methane production or possible emission scenarios where produced methane has not yet been released into the atmosphere and could be recovered or utilized directly using available technologies.

A major source of high concentrations of anthropogenic methane emissions is waste management, especially domestic sewage treatment and landfills, which accounts for 12% of global anthropogenic methane emissions.[122] Anaerobic digestion bacteria in sewage from underground pipes and egg-shaped digesters can convert organic matter into biogas, which can lead to safety issues.[153,154] Almost all process units in a

https://doi.org/10.1021/acsenvironau.3c00002
ACS Environ. Au 2023, 3, 252−276

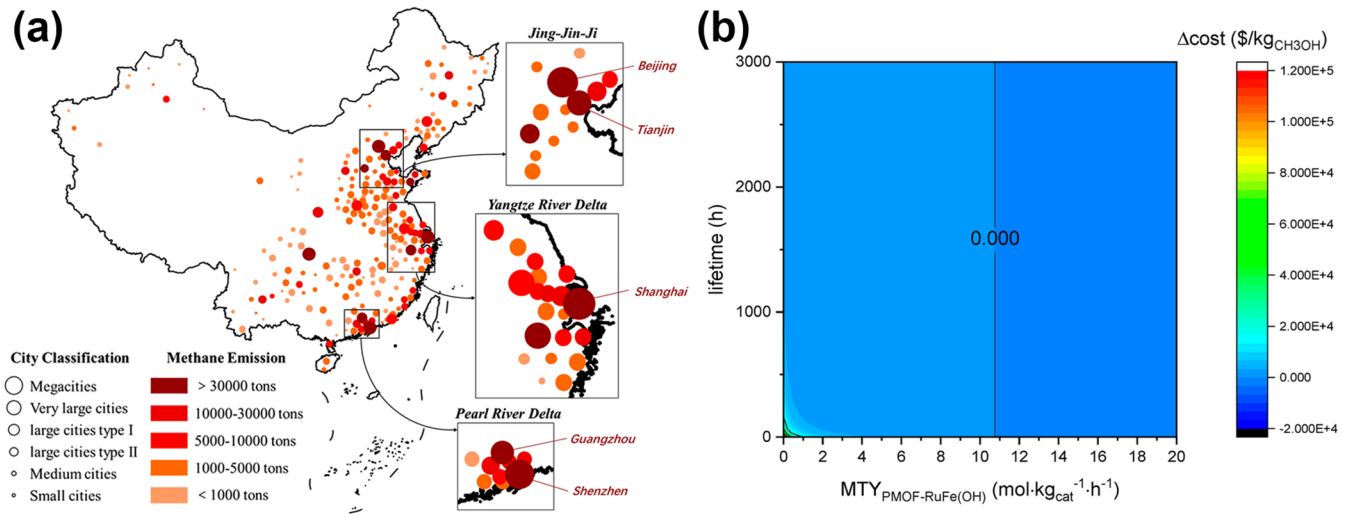

Figure 10. (a) CH_4 emissions from municipal wastewater treatment plants in 229 cities. Reprinted with permission.[156] Copyright 2019, Wiley-VCH. (b) Cost analysis of per kg methanol production by PMOF-RuFe(OH) photocatalysts. Reprinted with permission.[162] Copyright 2022, Springer Nature.

typical anaerobic/anoxic/oxic (A/A/O) municipal wastewater treatment plant (WWTP) emit methane, with anaerobic tanks, oxic tanks, aerated grit chambers, and sludge concentration tanks being major sources, accounting for 76−98% of total methane emissions in the A/A/O WWTPs.[155] Methane emissions from WWTPs increase with the demand for more influent. Total annual methane emissions from WWTPs in China were estimated to be around 1395.8 thousand tons (34.84 $MtCO_2e$) in 2014. More densely populated cities in the prosperous east are obviously the main contributors to methane emissions, possibly due to the adoption of more anaerobic treatment solutions for their WWTPs (Figure 10a).[156] In addition, the biodegradable organic matters in the waste will be decomposed by anaerobic bacteria to produce a mixture of biogases containing methane, especially for landfill gas (LFG), which generally contains about 50% CH_4, 50% CO_2, and a small amount of nonmethane organic compounds.[157] In China, the methane emissions from waste management reached 5.408 Mt yr^{-1} in 2017.[158] The common practice of burning LFG or biogas to generate electricity leads to 60−69 Mt yr^{-1} of CH_4 emissions, which is an unfavorable factor for climate greenhouse mitigation.[122]

In the oil and natural gas extraction process, associated gas and flare gas are valuable resources. Almost 150−170 billion m^3 yr^{-1} of gas is flared from production wells to generate 750 billion kWh of electricity, but this process is accompanied by 382 Mt yr^{-1} of CO_2 emissions and 3 Mt yr^{-1} of additional CH_4 emissions from unlit flaring.[159,160] Although the amounts of emitted CO_2 and CH_4 are minor in comparison to the gross reserves of atmospheric greenhouse gases, it will be beneficial if this part of methane in flare gas could be recovered. Conversions of methane to value-added chemicals provide commercially profitable paths for sustainable utilization of high concentrated methane. The use of flare gas as a feedstock to produce syngas and subsequent liquid fuels through Fischer−Tropsch (F−T) synthesis has been investigated and can recover at least 20% of unburnt methane.[161] However, such technologies still face challenges such as necessary methane purification, large storage facility footprints, and additional power consumption.

In situ resource upgrading technologies, represented by photocatalysis, have the potential to recover methane to value-added chemicals throughout the natural gas production end and replace cumbersome energy recovery.[49,105] Photocatalysis has been shown to be effective for the direct conversion of methane to methanol, ethylene, and benzene due to the rational design of active sites on catalyst surface. For concentrated methane, the advantages of photocatalysis over thermal catalysis are that (1) the carbon deposition of the photocatalyst is much more moderate than that of the thermal catalyst during long-term operation; and (2) the direct photocatalytic methane conversion can be carried out under ambient temperature (below 50 °C) or pressure (∼1 bar) without multistep F−T synthesis in the conventional process. Photocatalytic conversion of this high concentration methane to methanol exhibited good performance with a total methane conversion ratio exceeding 12% in pressurized batch reactors.[88] A total methane conversion ratio of 100% is also technically feasible if the residual gas can be recycled in better designed flow reactors. Recently, PMOF-RuFe(OH), a visible-light responsive photocatalyst composed of monoiron hydroxyl sites immobilized within a metal−organic framework, is used for partial POM with a substantial CH_3OH yield up to 8.81 mmol g^{-1} h^{-1} and corresponding CH_3OH selectivity is close to 100%.[162] Despite the relatively higher catalyst production costs, it is worth noting that the life cycle cost difference between this photocatalyst and ternary $Cu/ZnO/Al_2O_3$ (CZA) thermal catalysts can be smoothed out when the mass-time-yield (MTY) of CH_3OH is up to 10.7 mmol g^{-1} h^{-1}, as shown in Figure 10b.[162] This means that the further optimized PMOF-RuFe(OH) is able to compete against commercial CZA catalysts for the industrial synthesis of CH_3OH. In addition, the direct conversion of methane into multicarbon products is more preferred over methanol. Dehydrogenation coupling of methane to ethane and ethylene was achieved on ZnO nanorods loaded with Au−Pd core−shell nanorods, with a total methane conversion ratio of nearly 9.6% and a C_2H_4 yield and selectivity of 12.79 μmol g^{-1} h^{-1} and 39.7%, respectively, during the 8 h photocatalytic process.[106] However, the overall methane conversion ratio and C_2H_4 yields are still far from industrialization requirements (the

https://doi.org/10.1021/acsenvironau.3c00002
ACS Environ. Au 2023, 3, 252−276

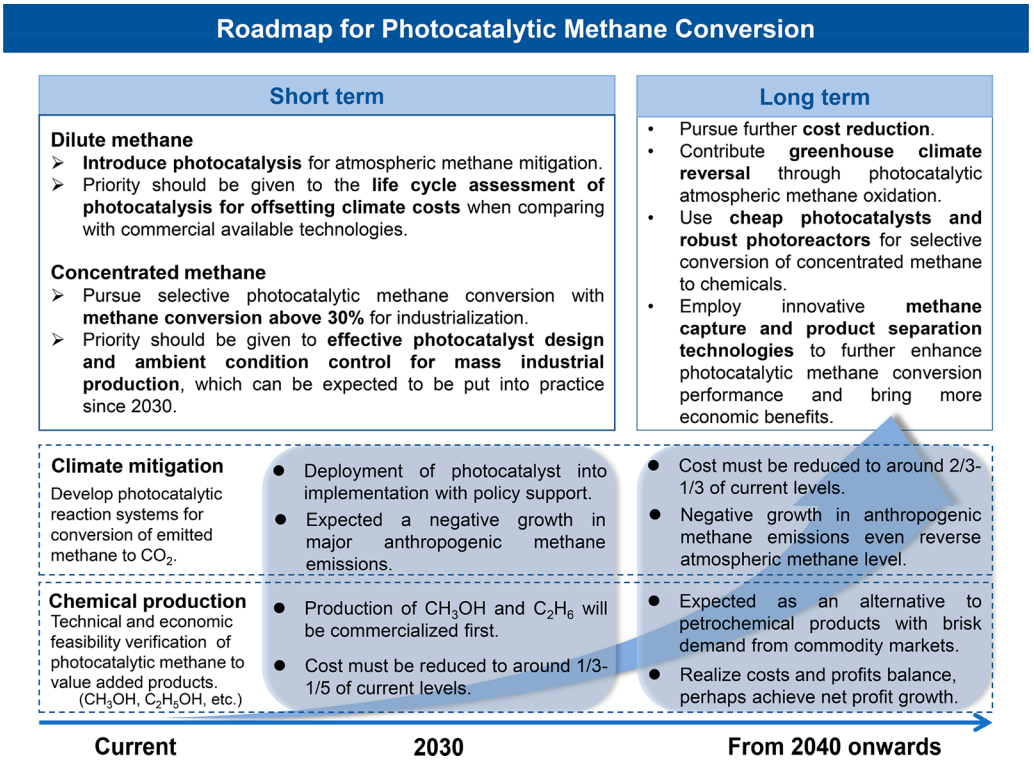

Figure 11. Roadmap of photocatalytic methane conversion technology for climate mitigation and chemical production.

methane conversion ratio should be above 30%), and the application of noble metals increases catalyst costs. Similarly, photocatalytic conversion of methane to ethanol has been reported in recent years, but this process faces the challenges of byproduct formation and inefficient methane conversion in the liquid phase.[83,163] At present, photocatalytic conversion of methane to products with industrial value is still in its infancy, and the problems described above have great potential for optimization. In order to successfully deploy photocatalytic conversion technology in high-concentration methane emission scenarios, it is important to design cheap and efficient catalysts, upgrade existing photoreactors, and build process prototype verification systems in future works.

5. CONCLUSIONS AND PERSPECTIVES

In the past 40 years, the dramatically increased methane concentration has given rise to air pollution (ozone) and global warming, resulting in rising concerns over human health, crop loss, and economic benefits as well. Therefore, we must pay intense attention to the mitigation of methane emissions. Photocatalytic methane conversion technologies stand for an encouraging prospect for lowering atmospheric methane concentration and converting methane to valuable chemicals. To improve the methane conversion efficiency and selectivity, strategies such as morphology control, heteroatom doping, facet engineering, cocatalysts modification, and utilization of electron scavengers have been proposed. These strategies can improve the conversion efficiency by enhancing the absorption of light, improving the separation efficiency of photogenerated carriers, and providing sites for methane adsorption and activation. As discussed in our article, the product selectivity in liquid−solid reaction systems can be altered not only by optimizing experimental factors (such as the amount of H_2O/O_2/H_2O_2, the light source, and the reaction time) but also by introducing active sites that can regulate the type and concentration of free radicals (mainly $^{\bullet}OH$ and $^{\bullet}OOH$), reduce the oxidation ability of holes, and regulate the breaking of specific chemical bond as well as the adsorption/desorption ability of intermediates. The improvement of C_2H_6 selectivity in gas−solid reaction systems can be achieved by using photocatalysts, which can suppress the combination of $*CH_3$ with *O and facilitate the desorption of C_2H_6. In addition, it is feasible to apply photocatalytic methane conversion technology to scenarios of diluted methane emission source and concentrated methane source. Photocatalytic oxidation of low-level or atmospheric-level methane to CO_2 gains opportunities for short-term climate mitigation, while photocatalytic conversions of concentrated methane to multicarbon products expand the pathways to achieve methane resource utilization in more sustainable and prospective approaches. With the demand for realizing a carbon-neutral society, this research field has attracted increasing attention recently. To promote the application of photocatalytic methane conversion technology in the industrial sector, we have listed the relative short-term targets for this technology by 2030 and medium- to long-term targets after 2040 (Figure 11). It is worth noting that although some encouraging results have been achieved in the field of photocatalytic methane conversion, the development of photocatalytic methane conversion is still in the preliminary stages, facing many challenges to be addressed, which are discussed in the following sections.

5.1. Design of Efficient Photocatalysts

Quantum efficiency (QE) is considered an important intrinsic parameter for evaluating the efficiency of photons-to-products. However, in the field of photocatalytic methane oxidation reactions, more than 50% of the work did not provide QE values. To date, the QE of photocatalytic methane conversion is mostly below 5%, and only a few works can reach above

https://doi.org/10.1021/acsenvironau.3c00002
ACS Environ. Au 2023, 3, 252−276

10%. More importantly, these values are obtained under ultraviolet light.[101,111,149,164] However, in the solar energy, the ratio of UV light (<400 nm) is less than 5%, while visible light (400−700 nm) and near-infrared (NIR) light (>700 nm) account for approximately 43% and 52%, respectively.[165] Therefore, extensive efforts require dedication to further improving the values of η_{abs}, η_{cs}, and η_{redox} and developing photocatalysts with high QE under visible light. In other photocatalytic reactions, such as photocatalytic CO_2 reduction reactions, the QE could reach 10% at 450 nm by accelerating the electron transfer between molecular catalysts and photosensitizers.[166] In photocatalytic hydrogen evolution reactions, introducing suitable donors and receptors into the covalent organic frameworks can extend the carrier lifetime and achieve a quantum yield of 82.6% at 450 nm after loading Pt cocatalyst.[167] Therefore, there is still a long way to go to improve the performance of photocatalytic methane conversion. In addition to several strategies showed in this review, constructing photocatalysts with heterojunction structure is also a promising way to promote charge carrier separation and improve the photon utilization efficiency, which has been extensively applied for photocatalytic water splitting,[168] CO_2 photoreduction,[169] and pollutant degradation.[170]

5.2. Exploration of Noble Metal-Free Cocatalysts

Most of the developed cocatalysts are noble-metal-based cocatalysts, which are difficult to apply in large scale due to their scarcity and expensiveness. Improving the atomic utilization efficiency of cocatalysts by controlling their characteristics (such as facet, size, structure, loading amount, and surface area) is an effective approach to lower the cost, but research exploring the effect of these characteristics on methane conversion performance is scare. There are a few examples of using single-atom (SA) cocatalysts with nearly 100% atomic efficiency in photocatalytic methane conversion, such as Pd SAs on TiO_2.[111] At the same time, it is crucial to seek noble-metal-free cocatalysts. The reported nonprecious cocatalyst, such as $SrCO_3$ (basic oxide), can facilitate the adsorption of methane (Lewis acid) by the acid−base interaction.[171,172] The decoration of iron species on TiO_2 can lower the energy barrier for H_2O_2 reduction, promoting the generation of $^{\bullet}OH$ radicals and methane activation.[108] These examples provide helpful guidance for the subsequent design of noble-metal-free cocatalysts.

5.3. Mechanistic Investigation of Photocatalytic Methane Conversion

Although similar photocatalysts are used, the proposed mechanism and pathway are very different. For instance, as for nonoxidative coupling of methane, methane molecules were reported to initially interact with semiconductors (such as ZnO) and oxidized by holes to generate $Zn-CH_3^{\bullet}$, which can interact with the second methane subsequently and form a $Zn-CH_3-CH_3$ intermediate, followed by the generation of C_2H_6.[173] However, some researchers suggested that methane molecules were reduced into CH_3^- anions by the photoinduced electrons on noble metal sites (such as Au). Thereafter, the CH_3^- anion migrated to TiO_2 and reacted with holes to generate $^{\bullet}CH_3$, which can produce C_2H_6 via self-coupling.[42] By using ZnO/Au as photocatalysts for liquid−solid reaction, Ye's group demonstrated that O_2 was the O-source for oxygenates generation (CH_3OOH, CH_3OH, and HCHO) through the reaction between $^{\bullet}CH_3$ and $^{\bullet}OOH$ (from O_2 reduction),[44] whereas Tang's group showed that both O_2 and H_2O are the O-source of CH_3OH because the $^{\bullet}CH_3$ radical can directly react with $^{\bullet}OH$ (from H_2O oxidation).[50] The observed differences may be related to experimental parameters such as the ratio of oxygen to methane, the loading amount of Au, or the water volume. Therefore, we need to combine a great deal of experimental and theoretical calculations to carefully determine the reaction mechanisms. Future work should pay attention to in situ/operando characterization techniques such as in situ DRIFTS, in situ ESR, and X-ray absorption techniques, which can provide a deep understanding of the key intermediates, the active species, and the real catalytic sites.

5.4. Application of Computational Chemistry and Machine Leaning in Catalysts Design

The incorporation of high-throughput experimental techniques with computational chemistry and machine learning (ML) holds significant promise for advancing the design of efficient photocatalysts.[19] This data-driven approach has the potential to bring about irreversible changes in the field of materials science research and development. However, there exist several challenges that need to be addressed to realize this potential. One of the major challenges is the acquisition of appropriate data sets, which is complicated by the fact that many material properties are process-dependent and researchers employ different protocols and conditions. Moreover, the properties of solid materials are not solely dependent on their chemical composition but also on the structures and morphologies of various scales, including higher-order structures of polymers, grain boundaries, and pores of inorganic materials. Density functional theory (DFT) has been employed for predicting new photocatalysts in recent years.[174] However, the number of compounds explored using this technique is significantly lower than the vast chemical space that exists. To augment and accelerate DFT calculations, ML has emerged as an attractive approach and is increasingly being used for predicting new photocatalysts and their properties. In general, a convolutional neural network is trained using a known synthesis to conduct high-throughput experiments. The obtained data is then used to generate a data set that links experimental and chemical parameters, which is subsequently utilized to train a tree-based ML regressor for further photocatalyst synthesis.[175] By optimizing the calculation methodologies, exploring the preparation of efficient photocatalysts and screening the conditions for the photocatalytic oxidation of methane using machine learning, we can expect to rapidly design highly efficient photocatalysts for the selective photooxidation of methane.

5.5. Put the Photocatalytic Methane Conversion into Practice

At present, most studies on photocatalytic methane conversion are based on pure methane, and the reaction conditions are too stable and perfect, which may mask the optimistic illusion of the development of this technology. However, the actual adverse factors, such as the variable concentration of actual methane flow, possible catalyst deactivation, and short solar illumination time, bring uncertainty to the application of photocatalytic methane conversion, prolong the time required for technology conversion, and greatly reduce the technical competitiveness. Therefore, we recommend that methane conversion be integrated into practical application scenarios as soon as possible. For example, the sewage treatment plant we mentioned earlier is an excellent "resource plant", where the

https://doi.org/10.1021/acsenvironau.3c00002
ACS Environ. Au 2023, 3, 252−276

anaerobic digester continuously produces biogas as a good source of methane, and the plant footprint also provides sufficient illumination area for the deployment of a large amount of photocatalysts without exaggerated facility upgrade costs, which not only generates positive revenue but also reduces greenhouse gas emissions. In addition, cross-disciplinary technical exchanges and support are critical to enable the development of photocatalytic technology applications to break through limitations. For example, the coupling of photocatalysis and purification technology may be one of the effective ways to reduce the cost and environmental risks of atmospheric methane conversion and reuse dormant atmospheric methane resources in the future. We hope that our insights will be validated in practical engineering in the future, and we look forward to more application-oriented research on photocatalytic methane conversion.

5.6. Techno-Economic Analyses of Photocatalytic Methane Conversion Systems

At present, research on photocatalytic methane oxidation needs to consider how to overcome the bottlenecks (catalysts, mechanisms, units, etc.) that limit further development of photocatalysis. The industry-oriented perspectives are recommended to evaluate how much contribution photocatalytic methane conversion can make to global energy conversion, methane mitigation, and even climate change. Techno-economic analysis (TEA) has been widely used in modern industry as one of the means to evaluate the commercial viability of catalysts. For the photocatalysis process, catalyst (synthesis cost, structure, active sites, lifetime), catalytic performance (methane conversion, target product selectivity, quantum efficiency), and reactor (design, production) are necessary factors in a complete TEA analysis process. Based on the above results, a feasible path for optimization of the catalytic system can be obtained. For example, the activation efficiency of photocatalytic methane limits the conversion of methane in the flow-cell device; future research should focus on developing efficient photocatalysts. Furthermore, cost estimates and trade-offs from the comparisons of timely methane abatement and post-treatment are also important indicators of TEA in determining the economic feasibility of the social cost of methane. It is hoped that the TEA analysis of photocatalytic methane oxidation can be used in subsequent works.

AUTHOR INFORMATION

Corresponding Author

Wenlei Zhu − *State Key Laboratory of Pollution Control and Resource Reuse, Frontiers Science Center for Critical Earth Material Cycling, School of the Environment and and State Key Laboratory of Analytical Chemistry for Life Science, School of Chemistry and Chemical Engineering, Nanjing University, Nanjing 210023, China;* orcid.org/0000-0001-6110-993X; Email: wenleizhu@nju.edu.cn

Authors

Zhuo Liu − *State Key Laboratory of Pollution Control and Resource Reuse, Frontiers Science Center for Critical Earth Material Cycling, School of the Environment and and State Key Laboratory of Analytical Chemistry for Life Science, School of Chemistry and Chemical Engineering, Nanjing University, Nanjing 210023, China*

Biyang Xu − *State Key Laboratory of Pollution Control and Resource Reuse, Frontiers Science Center for Critical Earth Material Cycling, School of the Environment and and State Key Laboratory of Analytical Chemistry for Life Science, School of Chemistry and Chemical Engineering, Nanjing University, Nanjing 210023, China*

Yu-Jing Jiang − *State Key Laboratory of Pollution Control and Resource Reuse, Frontiers Science Center for Critical Earth Material Cycling, School of the Environment and and State Key Laboratory of Analytical Chemistry for Life Science, School of Chemistry and Chemical Engineering, Nanjing University, Nanjing 210023, China*

Yang Zhou − *Key Laboratory for Organic Electronics & Information Displays (KLOEID), Institute of Advanced Materials (IAM), Nanjing University of Posts & Telecommunications (NJUPT), Nanjing 210046, China*

Xiaolian Sun − *State Key Laboratory of Natural Medicines, Key Laboratory of Drug Quality Control and Pharmacovigilance, Department of Pharmaceutics, China Pharmaceutical University, Nanjing 210009, China;* orcid.org/0000-0001-9549-4741

Yuanyuan Wang − *State Key Laboratory of Pollution Control and Resource Reuse, Frontiers Science Center for Critical Earth Material Cycling, School of the Environment and and State Key Laboratory of Analytical Chemistry for Life Science, School of Chemistry and Chemical Engineering, Nanjing University, Nanjing 210023, China;* orcid.org/0000-0003-3971-8362

Complete contact information is available at: https://pubs.acs.org/10.1021/acsenvironau.3c00002

Author Contributions

#All authors have given approval to the final version of the manuscript. Zhuo Liu and Biyang Xu contributed equally to this paper.

Notes

The authors declare no competing financial interest.

ACKNOWLEDGMENTS

The authors gratefully acknowledge the support from the National Natural Science Foundation of China (22176086, 22276100, 82272138, 22171132), the Natural Science Foundation of Jiangsu Province (BK20210189, SBK2022044384), State Key Laboratory of Pollution Control and Resource Reuse (PCRR-ZZ-202106), the Fundamental Research Funds for the Central Universities (021114380183, 021114380189, 021114380199), the Research Funds from Frontiers Science Center for Critical Earth Material Cycling of Nanjing University, Key Laboratory for Organic Electronics & Information Displays (GZR2022010010), Nanjing Science and Technology Innovation Project for Chinese Scholars Studying Abroad (NJKCZYZZ2022-01), Jiangsu Province Outstanding Youth Fund (BK20220086), Double first class Fund, China Pharmaceutical University (CPUQNJC22_03), the Zijin Scholars Foundation (0205181022), and Research Funds for Jiangsu Distinguished Professor.

REFERENCES

(1) Feng, J.-C.; Yan, J.; Wang, Y.; Yang, Z.; Zhang, S.; Liang, S.; Li, X.-S. Methane mitigation: Learning from the natural marine environment. *Innovation* **2022**, 3, No. 100297.

(2) Fu, J.; Li, P.; Lin, Y.; Du, H.; Liu, H.; Zhu, W.; Ren, H. Fight for carbon neutrality with state-of-the-art negative carbon emission technologies. *Eco-Environment & Health* **2022**, *1*, 259−279.
(3) Ming, T.; et al. Perspectives on removal of atmospheric methane. *Adv. Appl. Energy* **2022**, *5*, No. 100085.
(4) Rosentreter, J. A.; et al. Half of global methane emissions come from highly variable aquatic ecosystem sources. *Nat. Geosci.* **2021**, *14*, 225−230.
(5) Jackson, R. B.; et al. Increasing anthropogenic methane emissions arise equally from agricultural and fossil fuel sources. *Environ. Res. Lett.* **2020**, *15*, No. 071002.
(6) Voigt, C.; et al. Warming of subarctic tundra increases emissions of all three important greenhouse gases − carbon dioxide, methane, and nitrous oxide. *Global Change Biol.* **2017**, *23*, 3121−3138.
(7) West, J. J.; Fiore, A. M.; Horowitz, L. W.; Mauzerall, D. L. Global health benefits of mitigating ozone pollution with methane emission controls. *Proc. Natl. Acad. Sci. U. S. A.* **2006**, *103*, 3988−3993.
(8) United Nations Environment Programme. *Global Methane Assessment: Benefits and Costs of Mitigating Methane Emissions*. May 6, 2021.
(9) Nisbet, E. G.; Fisher, R. E.; Lowry, D.; France, J. L.; Allen, G.; Bakkaloglu, S.; Broderick, T. J.; Cain, M.; Coleman, M.; Fernandez, J.; et al. Methane mitigation: Methods to reduce emissions, on the path to the Paris Agreement. *Rev. Geophys.* **2020**, *58*, No. e2019RG000675.
(10) Krevor, S.; et al. Subsurface carbon dioxide and hydrogen storage for a sustainable energy future. *Nat. Rev. Earth Environ.* **2023**, *4*, 102−118.
(11) Du, F.; Nojabaei, B. A review of gas injection in shale reservoirs: Enhanced oil/gas recovery approaches and greenhouse gas control. *Energies* **2019**, *12*, 2355.
(12) Lee, S.-Y.; Lee, J.-U.; Lee, I.-B.; Han, J. Design under uncertainty of carbon capture and storage infrastructure considering cost, environmental impact, and preference on risk. *Appl. Energy* **2017**, *189*, 725−738.
(13) Jiang, X.; Mira, D.; Cluff, D. L. The combustion mitigation of methane as a non-CO_2 greenhouse gas. *Prog. Energy Combust. Sci.* **2018**, *66*, 176−199.
(14) Hu, W.; Lan, J.; Guo, Y.; Cao, X.; Hu, P. Origin to efficient catalytic combustion of methane over Co_3O_4 (110): Active low-coordination lattice oxygen and cooperation of multi active sites. *ACS Catal.* **2016**, *6*, 5508−5519.
(15) Tian, Y.; Piao, L.; Chen, X. Research progress on the photocatalytic activation of methane to methanol. *Green Chem.* **2021**, *23*, 3526−3541.
(16) Schwach, P.; Pan, X.; Bao, X. Direct conversion of methane to value-added chemicals over heterogeneous catalysts: Challenges and prospects. *Chem. Rev.* **2017**, *117*, 8497−8520.
(17) Song, H.; Meng, X.; Wang, Z.-j.; Liu, H.; Ye, J. Solar-energy-mediated methane conversion. *Joule* **2019**, *3*, 1606−1636.
(18) Bagherzadeh Mostaghimi, A. H.; Al-Attas, T. A.; Kibria, M. G.; Siahrostami, S. A review on electrocatalytic oxidation of methane to oxygenates. *J. Mater. Chem. A* **2020**, *8*, 15575−15590.
(19) Li, Q.; Ouyang, Y.; Li, H.; Wang, L.; Zeng, J. Photocatalytic conversion of methane: Recent advancements and prospects. *Angew. Chem., Int. Ed.* **2022**, *61*, No. e202108069.
(20) Brenneis, R. J.; Johnson, E. P.; Shi, W.; Plata, D. L. Atmospheric- and low-level methane abatement via an earth-abundant catalyst. *ACS Environ. Au* **2022**, *2*, 223−231.
(21) Angeli, S. D.; Monteleone, G.; Giaconia, A.; Lemonidou, A. A. State-of-the-art catalysts for CH_4 steam reforming at low temperature. *Int. J. Hydrogen Energy* **2014**, *39*, 1979−1997.
(22) Behrens, M.; et al. The active site of methanol synthesis over $Cu/ZnO/Al_2O_3$ industrial catalysts. *Science* **2012**, *336*, 893−897.
(23) Khodakov, A. Y.; Chu, W.; Fongarland, P. Advances in the development of novel cobalt Fischer−Tropsch catalysts for synthesis of long-chain hydrocarbons and clean fuels. *Chem. Rev.* **2007**, *107*, 1692−1744.
(24) Xie, S.; Lin, S.; Zhang, Q.; Tian, Z.; Wang, Y. Selective electrocatalytic conversion of methane to fuels and chemicals. *J. Energy Chem.* **2018**, *27*, 1629−1636.
(25) Qi, G.; et al. Au-ZSM-5 catalyses the selective oxidation of CH_4 to CH_3OH and CH_3COOH using O_2. *Nat. Catal.* **2022**, *5*, 45−54.
(26) Yuliati, L.; Yoshida, H. Photocatalytic conversion of methane. *Chem. Soc. Rev.* **2008**, *37*, 1592−602.
(27) Chen, Y.; et al. A robust fuel cell operated on nearly dry methane at 500 °C enabled by synergistic thermal catalysis and electrocatalysis. *Nat. Energy* **2018**, *3*, 1042−1050.
(28) Murcia-López, S.; Bacariza, M. C.; Villa, K.; Lopes, J. M.; Henriques, C.; Morante, J. R.; Andreu, T. Controlled photocatalytic oxidation of methane to methanol through surface modification of beta zeolites. *ACS Catal.* **2017**, *7*, 2878−2885.
(29) Zhou, L.; et al. Light-driven methane dry reforming with single atomic site antenna-reactor plasmonic photocatalysts. *Nat. Energy* **2020**, *5*, 61−70.
(30) Zheng, K.; et al. Room-temperature photooxidation of CH_4 to CH_3OH with nearly 100% selectivity over hetero-ZnO/Fe_2O_3 porous nanosheets. *J. Am. Chem. Soc.* **2022**, *144*, 12357−12366.
(31) Zhu, S.; et al. Efficient photooxidation of methane to liquid oxygenates over ZnO nanosheets at atmospheric pressure and near room temperature. *Nano Lett.* **2021**, *21*, 4122−4128.
(32) Zhu, Z.; Guo, W.; Zhang, Y.; Pan, C.; Xu, J.; Zhu, Y.; Lou, Y. Research progress on methane conversion coupling photocatalysis and thermocatalysis. *Carbon Energy* **2021**, *3*, 519−540.
(33) Du, J.; et al. Evoked methane photocatalytic conversion to C2 oxygenates over ceria with oxygen vacancy. *Catalysts* **2020**, *10*, 196.
(34) Li, F.; Cheng, L.; Fan, J.; Xiang, Q. Steering the behavior of photogenerated carriers in semiconductor photocatalysts: A new insight and perspective. *J. Mater. Chem. A* **2021**, *9*, 23765−23782.
(35) Chen, G.; et al. From solar energy to fuels: Recent advances in light-driven C1 chemistry. *Angew. Chem., Int. Ed.* **2019**, *58*, 17528−17551.
(36) Jiao, X.; Zheng, K.; Liang, L.; Li, X.; Sun, Y.; Xie, Y. Fundamentals and challenges of ultrathin 2D photocatalysts in boosting CO_2 photoreduction. *Chem. Soc. Rev.* **2020**, *49*, 6592−6604.
(37) Rueda-Marquez, J. J.; Levchuk, I.; Fernández Ibañez, P.; Sillanpää, M. A critical review on application of photocatalysis for toxicity reduction of real wastewaters. *J. Cleaner Prod.* **2020**, *258*, No. 120694.
(38) Jiang, Y.; Fan, Y.; Li, S.; Tang, Z. Photocatalytic methane conversion: Insight into the mechanism of $C(sp^3)$−H bond activation. *CCS Chem.* **2023**, *5*, 30−54.
(39) Sun, Z.; Wang, C.; Hu, Y. H. Highly selective photocatalytic conversion of methane to liquid oxygenates over silicomolybdic-acid/TiO_2 under mild conditions. *J. Mater. Chem. A* **2021**, *9*, 1713−1719.
(40) Meng, X.; Cui, X.; Rajan, N. P.; Yu, L.; Deng, D.; Bao, X. Direct methane conversion under mild condition by thermo-, electro-, or photocatalysis. *Chem.* **2019**, *5*, 2296−2325.
(41) Wei, S.; et al. Aerobic oxidation of methane to formaldehyde mediated by crystal-O over gold modified tungsten trioxide via photocatalysis. *Appl. Catal., B* **2021**, *283*, No. 119661.
(42) Lang, J.; Ma, Y.; Wu, X.; Jiang, Y.; Hu, Y. H. Highly efficient light-driven methane coupling under ambient conditions based on an integrated design of a photocatalytic system. *Green Chem.* **2020**, *22*, 4669−4675.
(43) Yang, J.; Hao, J.; Wei, J.; Dai, J.; Li, Y. Visible-light-driven selective oxidation of methane to methanol on amorphous FeOOH coupled m-WO_3. *Fuel* **2020**, *266*, No. 117104.
(44) Song, H.; Meng, X.; Wang, S.; Zhou, W.; Wang, X.; Kako, T.; Ye, J. Direct and selective photocatalytic oxidation of CH_4 to oxygenates with O_2 on cocatalysts/ZnO at room temperature in water. *J. Am. Chem. Soc.* **2019**, *141*, 20507−20515.
(45) Feng, G.; et al. Solar driven efficient direct conversion of methane to multicarbon oxygenates. *J. Mater. Chem. A* **2022**, *10*, 7856−7868.

https://doi.org/10.1021/acsenvironau.3c00002
ACS Environ. Au 2023, 3, 252−276

(46) Wu, S.; Wang, L.; Zhang, J. Photocatalytic non-oxidative coupling of methane: Recent progress and future. *J. Photochem. Photobiol., C* **2021**, *46*, No. 100400.
(47) Hu, D.; Ordomsky, V. V.; Khodakov, A. Y. Major routes in the photocatalytic methane conversion into chemicals and fuels under mild conditions. *Appl. Catal., B* **2021**, *286*, No. 119913.
(48) Sher Shah, M. S. A.; Oh, C.; Park, H.; Hwang, Y. J.; Ma, M.; Park, J. H. Catalytic oxidation of methane to oxygenated products: Recent advancements and prospects for electrocatalytic and photocatalytic conversion at low temperatures. *Adv. Sci.* **2020**, *7*, No. 2001946.
(49) Luo, L.; Gong, Z.; Xu, Y.; Ma, J.; Liu, H.; Xing, J.; Tang, J. Binary Au−Cu reaction sites decorated ZnO for selective methane oxidation to C1 oxygenates with nearly 100% selectivity at room temperature. *J. Am. Chem. Soc.* **2022**, *144*, 740−750.
(50) Zhou, W.; et al. Highly selective aerobic oxidation of methane to methanol over gold decorated zinc oxide via photocatalysis. *J. Mater. Chem. A* **2020**, *8*, 13277−13284.
(51) Song, H.; Meng, X.; Wang, S.; Zhou, W.; Song, S.; Kako, T.; Ye, J. Selective photo-oxidation of methane to methanol with oxygen over dual-cocatalyst-modified titanium dioxide. *ACS Catal.* **2020**, *10*, 14318−14326.
(52) Villa, K.; Murcia-López, S.; Andreu, T.; Morante, J. R. Mesoporous WO_3 photocatalyst for the partial oxidation of methane to methanol using electron scavengers. *Appl. Catal., B* **2015**, *163*, 150−155.
(53) Murcia-López, S.; Villa, K.; Andreu, T.; Morante, J. R. Partial oxidation of methane to methanol using bismuth-based photocatalysts. *ACS Catal.* **2014**, *4*, 3013−3019.
(54) Murcia-López, S.; Villa, K.; Andreu, T.; Morante, J. R. Improved selectivity for partial oxidation of methane to methanol in the presence of nitrite ions and $BiVO_4$ photocatalyst. *Chem. Commun.* **2015**, *51*, 7249−7252.
(55) Zhu, W.; et al. Facet-dependent enhancement in the activity of bismuth vanadate microcrystals for the photocatalytic conversion of methane to methanol. *ACS Appl. Nano Mater.* **2018**, *1*, 6683−6691.
(56) Wang, W.; Li, G.; Xia, D.; An, T.; Zhao, H.; Wong, P. K. Photocatalytic nanomaterials for solar-driven bacterial inactivation: Recent progress and challenges. *Environ. Sci.: Nano* **2017**, *4*, 782−799.
(57) Liang, Z.; Zheng, H.; Cao, R. Importance of electrocatalyst morphology for the oxygen reduction reaction. *ChemElectroChem.* **2019**, *6*, 2600−2614.
(58) Weiss, E. A. Designing the surfaces of semiconductor quantum dots for colloidal photocatalysis. *ACS Energy Lett.* **2017**, *2*, 1005−1013.
(59) Fan, Y.; et al. Selective photocatalytic oxidation of methane by quantum-sized bismuth vanadate. *Nat. Sustain.* **2021**, *4*, 509−515.
(60) Li, L.; Salvador, P. A.; Rohrer, G. S. Photocatalysts with internal electric fields. *Nanoscale* **2014**, *6*, 24−42.
(61) Ganguly, P.; et al. 2D nanomaterials for photocatalytic hydrogen production. *ACS Energy Lett.* **2019**, *4*, 1687−1709.
(62) Daulbayev, C.; Sultanov, F.; Bakbolat, B.; Daulbayev, O. 0D, 1D and 2D nanomaterials for visible photoelectrochemical water splitting. A review. *Int. J. Hydrogen Energy* **2020**, *45*, 33325−33342.
(63) Zhang, X.; Zhang, Z.; Wu, D.; Zhang, X.; Zhao, X.; Zhou, Z. Computational screening of 2D materials and rational design of heterojunctions for water splitting photocatalysts. *Small Methods* **2018**, *2*, No. 1700359.
(64) Sun, Z.; Talreja, N.; Tao, H.; Texter, J.; Muhler, M.; Strunk, J.; Chen, J. Catalysis of carbon dioxide photoreduction on nanosheets: Fundamentals and challenges. *Angew. Chem., Int. Ed.* **2018**, *57*, 7610−7627.
(65) Fu, J.; Yu, J.; Jiang, C.; Cheng, B. g-C_3N_4-based heterostructured photocatalysts. *Adv. Energy Mater.* **2018**, *8*, No. 1701503.
(66) Shi, S.; Sun, Z.; Bao, C.; Gao, T.; Hu, Y. H. The special route toward conversion of methane to methanol on a fluffy metal-free carbon nitride photocatalyst in the presence of H_2O_2. *Int. J. Energy Res.* **2020**, *44*, 2740−2753.
(67) Di, J.; Xia, J.; Li, H.; Liu, Z. Freestanding atomically-thin two-dimensional materials beyond graphene meeting photocatalysis: Opportunities and challenges. *Nano Energy* **2017**, *35*, 79−91.
(68) Sun, X.; Zhang, X.; Xie, Y. Surface defects in two-dimensional photocatalysts for efficient organic synthesis. *Matter* **2020**, *2*, 842−861.
(69) Wang, T.; et al. Recent advances on porous materials for synergetic adsorption and photocatalysis. *Energy Environ. Mater.* **2022**, *5*, 711−730.
(70) Sun, M.-H.; Huang, S.-Z.; Chen, L.-H.; Li, Y.; Yang, X.-Y.; Yuan, Z.-Y.; Su, B.-L. Applications of hierarchically structured porous materials from energy storage and conversion, catalysis, photocatalysis, adsorption, separation, and sensing to biomedicine. *Chem. Soc. Rev.* **2016**, *45*, 3479−3563.
(71) Chen, Z.; et al. Non-oxidative coupling of methane: N-type doping of niobium single atoms in TiO_2-SiO_2 induces electron localization. *Angew. Chem., Int. Ed.* **2021**, *60*, 11901−11909.
(72) Zhang, M.; He, L.; Shi, T.; Zha, R. Neat 3D C_3N_4 monolithic aerogels embedded with carbon aerogels via ring-opening polymerization with high photoreactivity. *Appl. Catal., B* **2020**, *266*, No. 118652.
(73) Zheng, K.; et al. Selective CH_4 partial photooxidation by positively charged metal clusters anchored on carbon aerogel under mild conditions. *Nano Lett.* **2021**, *21*, 10368−10376.
(74) Ma, J.; Long, R.; Liu, D.; Low, J.; Xiong, Y. Defect engineering in photocatalytic methane conversion. *Small Struct.* **2022**, *3*, No. 2100147.
(75) Chen, K.; et al. Zn dopants synergistic oxygen vacancy boosts ultrathin CoO layer for CO_2 photoreduction. *Adv. Funct. Mater.* **2022**, *32*, No. 2109336.
(76) Cheng, S.; et al. Emerging strategies for CO_2 photoreduction to CH_4: From experimental to data-driven design. *Adv. Energy Mater.* **2022**, *12*, No. 2200389.
(77) Jiang, C.; Moniz, S. J. A.; Wang, A.; Zhang, T.; Tang, J. Photoelectrochemical devices for solar water splitting − materials and challenges. *Chem. Soc. Rev.* **2017**, *46*, 4645−4660.
(78) Li, L.; Fan, S.; Mu, X.; Mi, Z.; Li, C. J. Photoinduced conversion of methane into benzene over GaN nanowires. *J. Am. Chem. Soc.* **2014**, *136*, 7793.
(79) Villa, K.; Murcia-López, S.; Morante, J. R.; Andreu, T. An insight on the role of La in mesoporous WO_3 for the photocatalytic conversion of methane into methanol. *Appl. Catal., B* **2016**, *187*, 30−36.
(80) Cheng, L.; Yin, H.; Cai, C.; Fan, J.; Xiang, Q. Single Ni atoms anchored on porous few-layer g-C_3N_4 for photocatalytic CO_2 reduction: The role of edge confinement. *Small* **2020**, *16*, No. 2002411.
(81) Chen, F.; Liu, L.-L.; Wu, J.-H.; Rui, X.-H.; Chen, J.-J.; Yu, Y. Single-atom iron anchored tubular g-C_3N_4 catalysts for ultrafast fenton-like reaction: Roles of high-valency iron-oxo species and organic radicals. *Adv. Mater.* **2022**, *34*, No. 2202891.
(82) Li, N.; Li, Y.; Jiang, R.; Zhou, J.; Liu, M. Photocatalytic coupling of methane and CO_2 into C2-hydrocarbons over Zn doped g-C_3N_4 catalysts. *Appl. Surf. Sci.* **2019**, *498*, No. 143861.
(83) Du, X.; Yang, Z.; Yang, X.; Zhang, Q.; Liu, L.; Ye, J. Efficient photocatalytic conversion of methane into ethanol over P-doped g-C_3N_4 under ambient conditions. *Energy Fuels* **2022**, *36*, 3929−3937.
(84) Agarwal, N.; et al. Aqueous Au-Pd colloids catalyze selective CH_4 oxidation to CH_3OH with O_2 under mild conditions. *Science* **2017**, *358*, 223−227.
(85) Zhou, Y.; Zhang, L.; Wang, W. Direct functionalization of methane into ethanol over copper modified polymeric carbon nitride via photocatalysis. *Nat. Commun.* **2019**, *10*, 506.
(86) Himes, R. A.; Barnese, K.; Karlin, K. D. One is lonely and three is a crowd: Two coppers are for methane oxidation. *Angew. Chem., Int. Ed.* **2010**, *49*, 6714−6716.
(87) Balasubramanian, R.; Smith, S. M.; Rawat, S.; Yatsunyk, L. A.; Stemmler, T. L.; Rosenzweig, A. C. Oxidation of methane by a biological dicopper centre. *Nature* **2010**, *465*, 115−119.

https://doi.org/10.1021/acsenvironau.3c00002
ACS Environ. Au 2023, 3, 252−276

(88) Xie, P.; Ding, J.; Yao, Z.; Pu, T.; Zhang, P.; Huang, Z.; Wang, C.; Zhang, J.; Zecher-Freeman, N.; Zong, H.; et al. Oxo dicopper anchored on carbon nitride for selective oxidation of methane. *Nat. Commun.* **2022**, *13*, 1375.
(89) Bai, S.; Wang, L.; Li, Z.; Xiong, Y. Facet-engineered surface and interface design of photocatalytic materials. *Adv. Sci.* **2017**, *4*, No. 1600216.
(90) Zhang, W.; et al. Crystal facet-dependent frustrated Lewis pairs on dual-metal hydroxide for photocatalytic CO_2 reduction. *Appl. Catal., B* **2022**, *300*, No. 120748.
(91) Ong, W.-J.; Tan, L.-L.; Chai, S.-P.; Yong, S.-T.; Mohamed, A. R. Facet-dependent photocatalytic properties of TiO_2-Based composites for energy conversion and environmental remediation. *ChemSusChem* **2014**, *7*, 690−719.
(92) Li, Z.; Boda, M. A.; Pan, X.; Yi, Z. Photocatalytic oxidation of small molecular hydrocarbons over ZnO nanostructures: The difference between methane and ethylene and the impact of polar and nonpolar facets. *ACS Sustainable Chem. Eng.* **2019**, *7*, 19042−19049.
(93) Luo, J.; Zhang, S.; Sun, M.; Yang, L.; Luo, S.; Crittenden, J. C. A critical review on energy conversion and environmental remediation of photocatalysts with remodeling crystal lattice, surface, and interface. *ACS Nano* **2019**, *13*, 9811−9840.
(94) Cheng, X.-M.; Zhao, J.; Sun, W.-Y. Facet-engineering of materials for photocatalytic application: Status and future prospects. *EnergyChem.* **2022**, *4*, No. 100084.
(95) Mu, L.; et al. Enhancing charge separation on high symmetry $SrTiO_3$ exposed with anisotropic facets for photocatalytic water splitting. *Energy Environ. Sci.* **2016**, *9*, 2463−2469.
(96) Liu, B.; et al. Charge separation between polar {111} surfaces of CoO octahedrons and their enhanced visible-light photocatalytic activity. *ACS Appl. Mater. Interfaces* **2015**, *7*, 6109−6117.
(97) Liu, G.; Yu, J. C.; Lu, G. Q.; Cheng, H.-M. Crystal facet engineering of semiconductor photocatalysts: Motivations, advances and unique properties. *Chem. Commun.* **2011**, *47*, 6763−6783.
(98) Chen, S.; et al. Facet-engineered surface and interface design of monoclinic scheelite bismuth vanadate for enhanced photocatalytic performance. *ACS Catal.* **2020**, *10*, 1024−1059.
(99) Villa, K.; Murcia-López, S.; Andreu, T.; Morante, J. R. On the role of WO_3 surface hydroxyl groups for the photocatalytic partial oxidation of methane to methanol. *Catal. Commun.* **2015**, *58*, 200−203.
(100) Ma, J.; et al. Efficient photoelectrochemical conversion of methane into ethylene glycol by WO_3 nanobar arrays. *Angew. Chem., Int. Ed.* **2021**, *60*, 9357−9361.
(101) Sun, X.; Chen, X.; Fu, C.; Yu, Q.; Zheng, X.-S.; Fang, F.; Liu, Y.; Zhu, J.; Zhang, W.; Huang, W. Molecular oxygen enhances H_2O_2 utilization for the photocatalytic conversion of methane to liquid-phase oxygenates. *Nat. Commun.* **2022**, *13*, 6677.
(102) Ran, J.; Jaroniec, M.; Qiao, S. Z. Cocatalysts in semiconductor-based photocatalytic CO_2 reduction: Achievements, challenges, and opportunities. *Adv. Mater.* **2018**, *30*, No. 1704649.
(103) Di, J.; et al. Cobalt nitride as a novel cocatalyst to boost photocatalytic CO_2 reduction. *Nano Energy* **2021**, *79*, No. 105429.
(104) Cheng, C.; et al. Facile preparation of nanosized MoP as cocatalyst coupled with g-C_3N_4 by surface bonding state for enhanced photocatalytic hydrogen production. *Appl. Catal., B* **2020**, *265*, No. 118620.
(105) Song, S.; et al. A selective Au-ZnO/TiO_2 hybrid photocatalyst for oxidative coupling of methane to ethane with dioxygen. *Nat. Catal.* **2021**, *4*, 1032−1042.
(106) Jiang, W.; et al. Pd-modified ZnO−Au enabling alkoxy intermediates formation and dehydrogenation for photocatalytic conversion of methane to ethylene. *J. Am. Chem. Soc.* **2021**, *143*, 269−278.
(107) Li, X.; Xie, J.; Rao, H.; Wang, C.; Tang, J. Platinum- and CuO_x-decorated TiO_2 photocatalyst for oxidative coupling of methane to C2 hydrocarbons in a flow reactor. *Angew. Chem., Int. Ed.* **2020**, *59*, 19702−19707.
(108) Xie, J.; et al. Highly selective oxidation of methane to methanol at ambient conditions by titanium dioxide-supported iron species. *Nat. Catal.* **2018**, *1*, 889−896.
(109) Ma, J.; Tan, X.; Zhang, Q.; Wang, Y.; Zhang, J.; Wang, L. Exploring the size effect of Pt nanoparticles on the photocatalytic nonoxidative coupling of methane. *ACS Catal.* **2021**, *11*, 3352−3360.
(110) Jiang, Y.; et al. Enabling specific photocatalytic methane oxidation by controlling free radical type. *J. Am. Chem. Soc.* **2023**, *145*, 2698−2707.
(111) Zhang, W.; Fu, C.; Low, J.; Duan, D.; Ma, J.; Jiang, W.; Chen, Y.; Liu, H.; Qi, Z.; Long, R.; et al. High-performance photocatalytic nonoxidative conversion of methane to ethane and hydrogen by heteroatoms-engineered TiO_2. *Nat. Commun.* **2022**, *13*, 2806.
(112) Tan, J. Z. Y.; Maroto-Valer, M. M. A review of nanostructured non-titania photocatalysts and hole scavenging agents for CO_2 photoreduction processes. *J. Mater. Chem. A* **2019**, *7*, 9368−9385.
(113) Das, R.; Chakraborty, S.; Peter, S. C. Systematic assessment of solvent selection in photocatalytic CO_2 reduction. *ACS Energy Lett.* **2021**, *6*, 3270−3274.
(114) Liang, L.; et al. Efficient infrared light induced CO_2 reduction with nearly 100% CO selectivity enabled by metallic CoN porous atomic layers. *Nano Energy* **2020**, *69*, No. 104421.
(115) Ding, X.; Song, L.; Han, Y.; Wang, Y.; Tang, X.; Cui, G.; Xu, Z. Effects of Fe^{3+} on acute toxicity and regeneration of planarian (*Dugesia japonica*) at different temperatures. *BioMed. Res. Int.* **2019**, *2019*, No. 8591631.
(116) Zuo, L.-Q.; Zhang, T.-F.; Zhang, Z.-K.; Hou, J.-X.; Liu, G.-J.; Du, J.-L.; Li, L.-J. A 3D binuclear salen-based multifunctional MOF: Degradation of MO dye and highly selective sensing of Fe^{3+}. *Inorg. Chem. Commun.* **2019**, *99*, 113−118.
(117) Zhao, S.; Song, X.; Chai, X.; Zhao, P.; He, H.; Liu, Z. Green production of fluorescent carbon quantum dots based on pine wood and its application in the detection of Fe^{3+}. *J. Cleaner Prod.* **2020**, *263*, No. 121561.
(118) Chen, Z.; Yao, D.; Chu, C.; Mao, S. Photocatalytic H_2O_2 production systems: Design strategies and environmental applications. *Chem. Eng. J.* **2023**, *451*, No. 138489.
(119) Liu, Y.; Zhu, Y.; Xu, J.; Bai, X.; Zong, R.; Zhu, Y. Degradation and mineralization mechanism of phenol by $BiPO_4$ photocatalysis assisted with H_2O_2. *Appl. Catal., B* **2013**, *142*, 561−567.
(120) López-Martín, Á.; Caballero, A.; Colón, G. Photochemical methane partial oxidation to methanol assisted by H_2O_2. *J. Photochem. Photobiol., A* **2017**, *349*, 216−223.
(121) Wang, Y.; Zhang, J.; Shi, W. X.; Zhuang, G. L.; Zhao, Q. P.; Ren, J.; Zhang, P.; Yin, H. Q.; Lu, T. B.; Zhang, Z. M. W single-atom catalyst for CH_4 photooxidation in water vapor. *Adv. Mater.* **2022**, *34*, No. e2204448.
(122) Saunois, M.; et al. The global methane budget 2000−2017. *Earth Syst. Sci. Data* **2020**, *12*, 1561−1623.
(123) Kirschke, S.; et al. Three decades of global methane sources and sinks. *Nat. Geosci.* **2013**, *6*, 813−823.
(124) Jackson, R. B.; et al. Increasing anthropogenic methane emissions arise equally from agricultural and fossil fuel sources. *Environ. Res. Lett.* **2020**, *15*, No. 071002.
(125) Bridgham, S. D.; Cadillo-Quiroz, H.; Keller, J. K.; Zhuang, Q. Methane emissions from wetlands: Biogeochemical, microbial, and modeling perspectives from local to global scales. *Global Change Biol.* **2013**, *19*, 1325−1346.
(126) Jackson, R. B.; et al. Atmospheric methane removal: A research agenda. *Philos. Trans. R. Soc., A* **2021**, *379*, No. 20200454.
(127) Karakurt, I.; Aydin, G.; Aydiner, K. Mine ventilation air methane as a sustainable energy source. *Renewable Sustainable Energy Rev.* **2011**, *15*, 1042−1049.
(128) Wang, X.; et al. Overview and outlook on utilization technologies of low-concentration coal mine methane. *Energy Fuels* **2021**, *35*, 15398−15423.
(129) Yang, Z.; et al. Enrichment of low concentration methane: An overview of ventilation air methane. *J. Mater. Chem. A* **2022**, *10*, 6397−6413.

(130) Bae, J.-S.; Su, S.; Yu, X. X. Enrichment of ventilation air methane (VAM) with carbon fiber composites. *Environ. Sci. Technol.* **2014**, *48*, 6043−6049.
(131) Cooper, J.; Balcombe, P.; Hawkes, A. The quantification of methane emissions and assessment of emissions data for the largest natural gas supply chains. *J. Cleaner Prod.* **2021**, *320*, No. 128856.
(132) Höglund-Isaksson, L. Bottom-up simulations of methane and ethane emissions from global oil and gas systems 1980 to 2012. *Environ. Res. Lett.* **2017**, *12*, No. 024007.
(133) Zhang, B.; Chen, G. Q.; Li, J. S.; Tao, L. Methane emissions of energy activities in China 1980−2007. *Renewable Sustainable Energy Rev.* **2014**, *29*, 11−21.
(134) Jackson, R. B.; Down, A.; Phillips, N. G.; Ackley, R. C.; Cook, C. W.; Plata, D. L.; Zhao, K. Natural gas pipeline leaks across Washington, DC. *Environ. Sci. Technol.* **2014**, *48*, 2051−2058.
(135) Yusuf, R. O.; Noor, Z. Z.; Abba, A. H.; Hassan, M. A. A.; Din, M. F. M. Methane emission by sectors: A comprehensive review of emission sources and mitigation methods. *Renewable Sustainable Energy Rev.* **2012**, *16*, 5059−5070.
(136) Zhou, X.; et al. Mobile measurement system for the rapid and cost-effective surveillance of methane and volatile organic compound emissions from oil and gas production sites. *Environ. Sci. Technol.* **2021**, *55*, 581−592.
(137) Ravikumar, A. P.; et al. Repeated leak detection and repair surveys reduce methane emissions over scale of years. *Environ. Res. Lett.* **2020**, *15*, No. 034029.
(138) Moss, A. R.; Jouany, J. P.; Newbold, J. Methane production by ruminants: Its contribution to global warming. *Ann. Zootech.* **2000**, *49*, 231−253.
(139) Smith, P.; et al. Greenhouse gas mitigation in agriculture. *Philos. Trans. R. Soc., B* **2008**, *363*, 789−813.
(140) Grainger, C.; Beauchemin, K. A. Can enteric methane emissions from ruminants be lowered without lowering their production? *Anim. Feed Sci. Technol.* **2011**, *166−167*, 308−320.
(141) Cao, Y.; Takahashi, T.; Horiguchi, K. i.; Yoshida, N.; Cai, Y. Methane emissions from sheep fed fermented or non-fermented total mixed ration containing whole-crop rice and rice bran. *Anim. Feed Sci. Technol.* **2010**, *157*, 72−78.
(142) Chen, W.; et al. Effects of different types of biochar on methane and ammonia mitigation during layer manure composting. *Waste Manage.* **2017**, *61*, 506−515.
(143) Bayat, A. R.; Tapio, I.; Vilkki, J.; Shingfield, K. J.; Leskinen, H. Plant oil supplements reduce methane emissions and improve milk fatty acid composition in dairy cows fed grass silage-based diets without affecting milk yield. *J. Dairy Sci.* **2018**, *101*, 1136−1151.
(144) Bačėninaitė, D.; Džermeikaitė, K.; Antanaitis, R. Global warming and dairy cattle: How to control and reduce methane emission. *Animals* **2022**, *12*, 2687.
(145) Narine, K.; Mahabir, J.; Koylass, N.; Samaroo, N.; Singh-Gryzbon, S.; Baboolal, A.; Guo, M.; Ward, K. Climate smart process design for current and future methanol production. *J. CO_2 Utili.* **2021**, *44*, No. 101399.
(146) Dalena, F.; Senatore, A.; Marino, A.; Gordano, A.; Basile, M.; Basile, A. Methanol production and applications: An overview. *Methanol* **2018**, 3−28.
(147) Sehested, J. Industrial and scientific directions of methanol catalyst development. *J. Catal.* **2019**, *371*, 368−375.
(148) Li, Z.; Pan, X.; Yi, Z. Photocatalytic oxidation of methane over CuO-decorated ZnO nanocatalysts. *J. Mater. Chem. A* **2019**, *7*, 469−475.
(149) Chen, X.; Li, Y.; Pan, X.; Cortie, D.; Huang, X.; Yi, Z. Photocatalytic oxidation of methane over silver decorated zinc oxide nanocatalysts. *Nat. Commun.* **2016**, *7*, 12273.
(150) de Richter, R.; Ming, T. Z.; Davies, P.; Liu, W.; Caillol, S. Removal of non-CO_2 greenhouse gases by large-scale atmospheric solar photocatalysis. *Prog. Energy Combust. Sci.* **2017**, *60*, 68−96.
(151) Ming, T.; et al. A novel green technology: Reducing carbon dioxide and eliminating methane from the atmosphere. *Int. J. Energy Res.* **2022**, *46*, 20107−20120.
(152) Johannisson, J.; Hiete, M. Exploring the photocatalytic total oxidation of methane through the lens of a prospective LCA. *Atmos. Environ.: X* **2022**, *16*, No. 100190.
(153) Guisasola, A.; de Haas, D.; Keller, J.; Yuan, Z. Methane formation in sewer systems. *Water Res.* **2008**, *42*, 1421−1430.
(154) Liu, Y. W.; Ni, B. J.; Sharma, K. R.; Yuan, Z. G. Methane emission from sewers. *Sci. Total Environ.* **2015**, *524*, 40−51.
(155) Wang, J.; Zhang, J.; Xie, H.; Qi, P.; Ren, Y.; Hu, Z. Methane emissions from a full-scale A/A/O wastewater treatment plant. *Bioresour. Technol.* **2011**, *102*, 5479−5485.
(156) Zhao, X.; et al. China's urban methane emissions from municipal wastewater treatment plant. *Earths Future* **2019**, *7*, 480−490.
(157) Themelis, N. J.; Ulloa, P. A. Methane generation in landfills. *Renewable Energy* **2007**, *32*, 1243−1257.
(158) Bian, R. X.; et al. Greenhouse gas emissions from waste sectors in China during 2006−2019: Implications for carbon mitigation. *Process Saf. Environ. Prot.* **2022**, *161*, 488−497.
(159) Tahmasebzadehbaie, M.; Sayyaadi, H. Technoeconomical, environmental, and reliability assessment of different flare gas recovery technologies. *J. Cleaner Prod.* **2022**, *367*, No. 133009.
(160) Hagos, F. Y.; Abd Aziz, A. R.; Zainal, E. Z.; Mofijur, M.; Ahmed, S. F. Recovery of gas waste from the petroleum industry: A review. *Environ. Chem. Lett.* **2022**, *20*, 263−281.
(161) Khalili-Garakani, A.; Nezhadfard, M.; Iravaninia, M. Enviro-economic investigation of various flare gas recovery and utilization technologies in upstream and downstream of oil and gas industries. *J. Cleaner Prod.* **2022**, *346*, No. 131218.
(162) An, B.; et al. Direct photo-oxidation of methane to methanol over a mono-iron hydroxyl site. *Nat. Mater.* **2022**, *21*, 932−938.
(163) Yang, Z.; Zhang, Q.; Ren, L.; Chen, X.; Wang, D.; Liu, L.; Ye, J. Efficient photocatalytic conversion of CH_4 into ethanol with O_2 over nitrogen vacancy-rich carbon nitride at room temperature. *Chem. Commun.* **2021**, *57*, 871−874.
(164) Yu, X.; De Waele, V.; Lofberg, A.; Ordomsky, V.; Khodakov, A. Y. Selective photocatalytic conversion of methane into carbon monoxide over zinc-heteropolyacid-titania nanocomposites. *Nat. Commun.* **2019**, *10*, 700.
(165) Li, G.; Guo, C.; Yan, M.; Liu, S. $CsxWO_3$ nanorods: Realization of full-spectrum-responsive photocatalytic activities from UV, visible to near-infrared region. *Appl. Catal., B* **2016**, *183*, 142−148.
(166) Wang, J.-W.; Jiang, L.; Huang, H.-H.; Han, Z.; Ouyang, G. Rapid electron transfer via dynamic coordinative interaction boosts quantum efficiency for photocatalytic CO_2 reduction. *Nat. Commun.* **2021**, *12*, 4276.
(167) Li, C.; Liu, J.; Li, H.; Wu, K.; Wang, J.; Yang, Q. Covalent organic frameworks with high quantum efficiency in sacrificial photocatalytic hydrogen evolution. *Nat. Commun.* **2022**, *13*, 2357.
(168) Moniz, S. J. A.; Shevlin, S. A.; Martin, D. J.; Guo, Z.-X.; Tang, J. Visible-light driven heterojunction photocatalysts for water splitting-a critical review. *Energy Environ. Sci.* **2015**, *8*, 731−759.
(169) Zhang, G.; Wang, Z.; Wu, J. Construction of a Z-scheme heterojunction for high-efficiency visible-light-driven photocatalytic CO_2 reduction. *Nanoscale* **2021**, *13*, 4359−4389.
(170) Chen, M.; Guo, C.; Hou, S.; Lv, J.; Zhang, Y.; Zhang, H.; Xu, J. A novel Z-scheme AgBr/P-g-C_3N_4 heterojunction photocatalyst: Excellent photocatalytic performance and photocatalytic mechanism for ephedrine degradation. *Appl. Catal., B* **2020**, *266*, No. 118614.
(171) Zhang, W.; Yu, Y.; Yi, Z. Controllable synthesis of $SrCO_3$ with different morphologies and their co-catalytic activities for photocatalytic oxidation of hydrocarbon gases over TiO_2. *J. Mater. Sci.* **2017**, *52*, 5106−5116.
(172) Pan, X.; Chen, X.; Yi, Z. Photocatalytic oxidation of methane over $SrCO_3$ decorated $SrTiO_3$ nanocatalysts via a synergistic effect. *Phys. Chem. Chem. Phys.* **2016**, *18*, 31400−31409.
(173) Meng, L.; et al. Gold plasmon-induced photocatalytic dehydrogenative coupling of methane to ethane on polar oxide surfaces. *Energy Environ. Sci.* **2018**, *11*, 294−298.

https://doi.org/10.1021/acsenvironau.3c00002
ACS Environ. Au 2023, 3, 252−276

(174) Jinnouchi, R.; Asahi, R. Predicting catalytic activity of nanoparticles by a DFT-aided machine-learning algorithm. *J. Phys. Chem. Lett.* **2017**, *8*, 4279−4283.
(175) Kirman, J.; et al. Machine-learning-accelerated perovskite crystallization. *Matter* **2020**, *2*, 938−947.

https://doi.org/10.1021/acsenvironau.3c00002
ACS Environ. Au 2023, 3, 252−276